10-19-2018

An Etching Study for Self-Aligned Double Patterning

Christopher O'Connell
cxo9160@rit.edu

An Etching Study for Self-Aligned Double Patterning

Christopher O'Connell
October 19,2018

A Thesis Submitted
in Partial Fulfillment
of the Requirements for the Degree of
Master of Science
in
Microelectronic Engineering

R·I·T | Kate Gleason *College of* ENGINEERING

Department of Electrical and Microelectronic Engineering

An Etching Study for Self-Aligned Double Patterning

Christopher O'Connell

A Thesis Submitted
in Partial Fulfillment
of the Requirements for the Degree of
Master of Science
in
Microelectronic Engineering

Committee Approval:

Dr. Robert Pearson *Advisor* Date
Program Director, Microelectronic Engineering

Dr. Karl Hirschman Date
Professor, Electrical and Microelectronic Engineering

Dr. Michael Jackson Date
Professor, Electrical and Microelectronic Engineering

Dr. Sohail Dianat Date
Deptartment Head, Electrical and Microelectronic Engineering

DEPARTMENT OF ELECTRICAL AND MICROELECTRONIC ENGINEERING
KATE GLEASON COLLEGE OF ENGINEERING
ROCHESTER INSTITUTE OF TECHNOLOGY
ROCHESTER, NEW YORK
October 19,2018

Acknowledgments

I would like to thank and acknowledge everyone who has helped and supported me throughout this process. Firstly, I would like to thank my committee members, Dr. Robert Pearson, Dr. Karl Hirschman and Dr. Michael Jackson for all their support and guidance throughout my time at RIT. A special thanks to Dr. Hirschman and the many members of Team Eagle over the years many of whom taught me a great number of things and trained me on tools. It was a pleasure to work with the SMFL Staff, Bruce Tolleson, Rich Battaglia, Zachary Kogut, Sean O'Brien, Scott Blondell and last but certainly not least Patricia Meller and John Nash. A special thanks goes to Patricia for our many conversations over the years about a variety of things but largely for helping me out when I needed it most and teaching me to be the process engineer I am today. Without John this project would have failed before it had started, beyond that his insights into how tools are intended to be run and how to diagnose process problems from tool problems as well as life advice has been invaluable. A very special thanks to Emily Shriver, for letting me stay at her apartment significantly longer than a month, being patient and putting up with me for the past year and few months. I would also like to thank Jeff Salzmann for his life advise and helping me with interviewing and career advice. I would also like to thank the grad office both old and new for their thoughtful discussions and being there for me when I needed to work something out, especially Venkatesh Deenadayalan who has listened to way too many of my ramblings and helped me work through problems I was stuck on. Lastly to all my family and friends I've made along the way I want to thank you for being there when I needed you and help make me the person I am today.

Abstract

A proposed process flow for a complete FinFET etch module is presented as well as experiments to ensure that the target films are etched uniformly with proper rate, selectivity and anisotropy. The proposed process flow was developed at RIT, designed to closely reproduce what the semiconductor industry uses for a Self-Aligned Double Patterning (SADP) process module while advancing RIT's current cleanroom facility capabilities.

The etching experiment is proposed such that a sufficient degree of etch endpoint control can be achieved without a spectrophotometer for endpoint detection using the Magnetically Enhanced Reactive Ion Etching (MERIE) system at RIT. Without the proper etch data a number of critical steps would be incredibly difficult to control. Prior to this work across wafer etch non-uniformity was reported to be approximately 10% with a regular rate of 1400-1500Å min^{-1}. This was improved through various means to a non-uniformity of $< 1\%$ and a rate of 2200Å min^{-1} on average. A way to achieve the mandrel etch and strip using gas ratios of 4:2:1::CF_4 :CHF_3 :C_2F_6 and 4:1::CHF_3 :C_2F_6 , was derived, respectively.

Contents

List of Figures

List of Tables

List of CVD and RIE Symbols

Term	Description	Units/Value
a_i	Thermodynamic concentration	
$a_{i(eq)}$	Thermodynamic concentration at equilibrium	
D_A	Radical diffusion coefficient	$\mathrm{m^3\,s^{-3}}$
D_a	Ambipolar diffusion coefficient	$\mathrm{m^3\,s^{-3}}$
d	Electrode separation distance	cm
G	Gibbs free energy	J
Gr_t	Grashoff's number (thermal)	$10^{-2} \leq 10^{2}$(APCVD)/ $0 \leq 10$(LPCVD)
g	Gravitational constant	$9.8\mathrm{m\,s^{-2}}$
H	Enthalpy	J
Kn	Knudsen number	$10^{-6} \leq 10^{-5}$(APCVD)/ $10^{-3} \leq 10^{-2}$(LPCVD)
L	Characteristic length	m
n_A	Radical density	$\mathrm{m^{-3}}$
n_i	Ion density	$\mathrm{m^{-3}}$
n_{mat}	Particle Density	$\mathrm{m^{-3}}$
p	Pressure	Pa
Re	Renyolds number	$10^{-2} \leq 10^{2}$
S	Entropy	$\mathrm{J\,K^{-1}}$
s_{rec}	Solid recombination probability	
T	Temperature	K
T_r	Reference Temperature	K
U	Internal Energy	J
V	Volume	$\mathrm{m^3}$
$\boldsymbol{V}$	Voltage	V
v	Velocity	$\mathrm{m\,s^{-1}}$
$\bar{v}$	Average speed	$\mathrm{m\,s^{-1}}$
α	Townsend Coefficient	$\#$ ions $\mathrm{m^{-1}}$
Γ	Particle flux	$\mathrm{m^{-2}\,s^{-1}}$

Term	Description	Units/Value
Γ_i	Positive ion particle flux	$\mathrm{m}^{-2}\,\mathrm{s}^{-1}$
η	Viscosity	Pa s
λ	Mean free path length	m
ρ	Density	$\mathrm{kg}\,\mathrm{m}^{-3}$

List of Anisotropy and Selectivity Symbols

Term	Description	Units/Value
A	Anisotropy	$(0 \leq 1)$
A_m	Mask anisotropy	$(0 \leq 1)$
B	Undercutting Bias	$(0 \leq 1)$
d_c	Minimum resolvable mask feature size/ Critical dimension (space)	µm
d_f	Desired feature size upper width	µm
d_m	Mask dimension(line)	µm
d_{Pitch}	Mask pitch	µm
R_f	Film etch rate	$\mu m\, s^{-1}$
R_h	Horizontal etch rate	$\mu m\, s^{-1}$
R_v	Mask erosion rate, Vertical etch rate	$\mu m\, s^{-1}$
$R_{v,ave}$	Average R_v	$\mu m\, s^{-1}$
R_s	Substrate erosion rate	$\mu m\, s^{-1}$
S_f^m	Selectivity of the mask to the film	$(0 \leq 1)$
S_s^f	Selectivity of the film to the substrate	$(0 \leq 1)$
t_c	Time to clear	s
t_{min}	Time until the substrate is first exposed to the plasma	s
t_{tot}	Total etch time	s
U_f^m	Uniformity factor for the film to the mask	$(0 \leq 1)$
U_s^f	Uniformity factor for the substrate to film	$(0 \leq 1)$
y_f	Film thickness	µm
$y_{s,max}$	Substrate max etch depth	µm
α	Film thickness variation	$(0 \leq 1)$
β	Film etch uniformity/variation	$(0 \leq 1)$
Δ	Mask erosion	µm
δ	Overetching parameter	$(0 \leq 1)$
ϵ	Mask erosion rate variation	$(0 \leq 1)$
θ	Mask angle	°

Motivation for a Patterning Etch Study

RIT has been teaching students about IC fabrication since the program's inception in 1982, the introduction of the masters program in 1987 and its student-run factory in 1988 [1–3]. In 1992 RIT accomplished a longterm goal of producing CMOS circuits for its factory class with a P-Well 9 photolithographic layer process and single level metal [1, 4]. This process was refined not much later in 2000 into a sub-micron process producing an $L_{eff} < 1.0$µm process with 10 lithographic levels and the introduction of a second metal layer [5, 6]. This process was then refined again to produce 250nm transistors in 2006 [7]. In 2014 this process was brought down to a 150nm advanced CMOS with a 14 level lithographic process [8–10].

In recent years industry has moved away from a planar structure, as shown in Figure 1.1a, that RIT has been using, and has moved to the FinFET device architecture as shown in Figure 1.1b [11, 12]. This is largely in part due to Moore's law moving the industry to make smaller and smaller transistors improving packing density. With this new development also comes larger control with the process, with planar devices the active area is simply $L * W$, however the active area in a FinFET is $L * (t + 2 * H_{fin})$ this allows for the transistor width to be dependent on height and minimally the width of the fin itself.

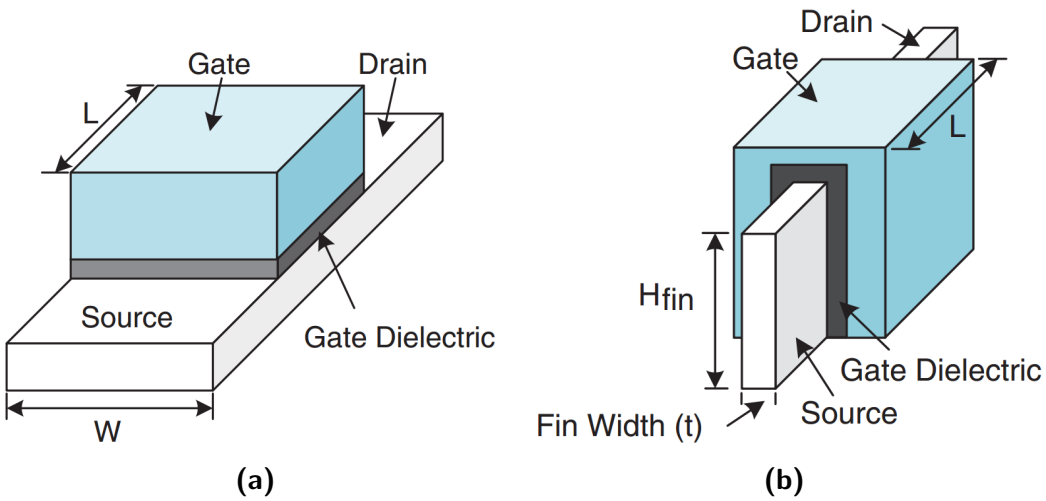

Figure 1.1: Two types of MOSFET: Planar FET(a) and FinFET(b) [11].

With this recent development in industry RIT is looking to further develop its CMOS process into a FinFET process. This has been attempted before at RIT using Low Temperature Oxide (LTO) sidewall spacers with a pitch of 0.5-1µm between fins [13–15]. While the process is sound, it doesn't have the appropriate packing density to call it a FinFET process. In order to continue forward, sub-lithographic patterning techniques, such as double patterning, need to be introduced.

There are multiple ways to go about sub-lithographic patterning primarily Litho-Etch-Litho-Etch (LELE), Litho-Freeze-Litho-Etch (LFLE) and Self-Aligned Double Patterning (SADP), these three techniques have been used at RIT with varying success [16–19]. As opposed to LELE and LFLE this work will primarily focus on SADP as a viable method for double patterning, primarily as it is likely to be the most expandable for a quadruple or even octuple patterning process. In the SADP process one of the key challenges is having a appropriate etch and deposition control as opposed to the lithographic concerns. A highly simplified SADP process is is depicted in 1.2 for the formation of a fin.

Without adequate hardmask and spacer definition etch processes, SADP becomes orders of magnitude more difficult. Spacer definition is simply depicted in Figure

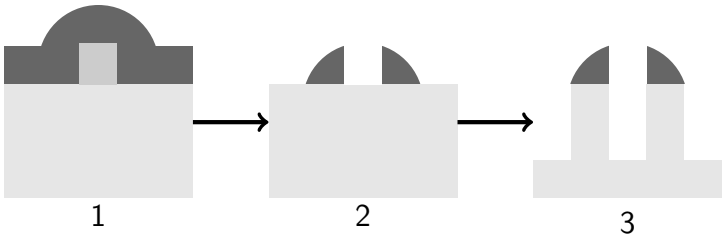

Figure 1.2: Simplified FinFET formation through SADP.

1.2, steps 1 and 2, whereas the hardmask problem is depicted primarily in step 3. For the fin-definition (step 3) a highly anisotropic etch must be performed to produce at least a 1:3 to 1:5 ratio for $t : H_{fin}$ (fin aspect ratio, as defined in Figure 1.1b). This requires that a highly selective and robust hardmask etch process be utilized. RIT has followed various industry practices in developing our own process for using carbon as a hardmask, be-it a-carbon/diamond-like carbon or Spin-On Carbon (SOC) [20, 21]. In order to further improve the RIT capabilities through development of a SADP process, both deposition and etching improvements must be accomplished to achieve a fin etch for FET construction. On the etch side of the process development significant studies of the oxide, hardmask, nitride and silicon etch capabilities all need to be carried out, each of which must address target material etch rate, etch selectivity, etch anisotropy and uniformity. A particular focus of this work is the oxide etch issues which appear in multiple steps within the process, namely in the mandrel etch and the mandrel removal explored in further detail in sections 3.1.6 and 3.1.9.

Lithography, Plasma Deposition and Etching Theory

2.1 Lithography

Semiconductor technology is driven by producing ever smaller features. Reducing the source wavelength is the easiest method of achiving smaller features. Originally industry intended to switch to an Extreme Ultraviolet (EUV) source with a 13.5 nm wavelength past the 193 nm node. Due to significant complications in the majority of steps in implementation as well as cost EUV has however been in perpetual development. As such to continue Moore's Law steps needed to be taken to produce smaller features without changing the source. Many ways have been developed such as Phase Shift Mask (PSM) and Optical Proximity Correction (OPC) but they only went so far. Even those techniques have stopped producing smaller features, new techniques needed to be developed. This is where Multiple patterning strategies have been conceived. Of these, two have become dominant to produce smaller features, LELE and SADP or variants thereof. The overall idea is to reduce the half-pitch(the length of line or space within a given pitch) to sub-wavelength levels through means of further lithography deposition and etching processes. SADP combines conventional optical lithography with deposition and etch steps to determine final feature dimensions, whereas LELE is primarily a lithographic process.

2.1.1 Litho-Etch-Litho-Etch

LELE is a lithography process where a pattern is formed from multiple patterning and direct etching steps. Both dense and isolated features can be formed from this technique. Generally metals with different etch properties such as aluminum and molybdenum are used as a hardmask, but other materials can also be used [17]. Figure 2.1 depicts a simplified process flow for LELE to produce dense 1:1 line:space features. As shown in

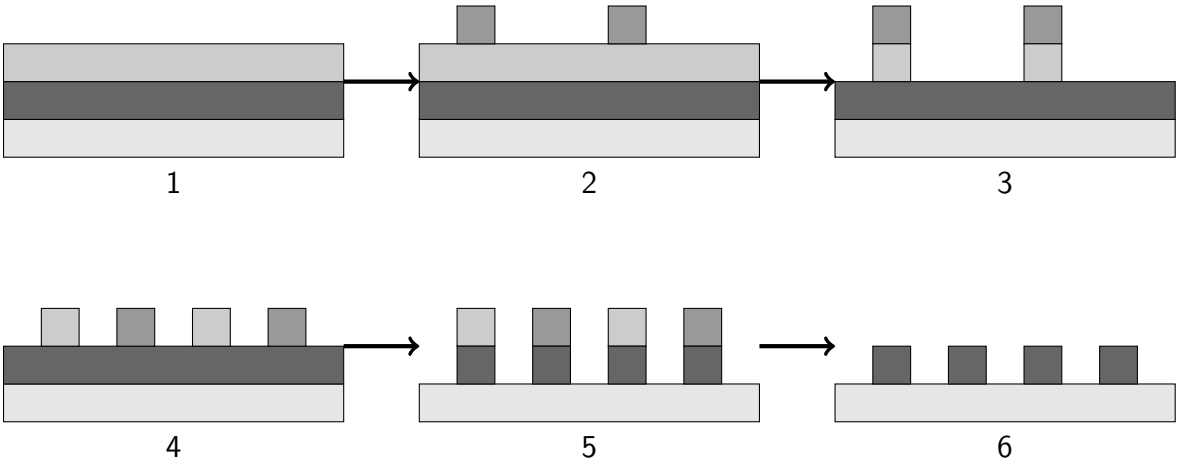

Figure 2.1: LELE Dense process flow(1:1) [17]

Figure 2.1, the general concept is to deposit the primary hardmask with a secondary hardmask above, depicted in Figure 2.1(1). Then photoresist is applied and patterned at a 1:3 line:space ratio to pattern the top hardmask as shown in Figure 2.1(2-3). Following this, more photoresist is applied and patterned again at the same pitch but with the line placed in the middle of the previous space as shown in Figure 2.1(4). This new photoresist layer and the top hardmask then are used to pattern the primary bottom hardmask as shown in Figure 2.1(5), where the top hardmask and photoresist are then removed leaving only the bottom hardmask as shown in Figure 2.1(6) [17, 22–24]. While LELE can produce good results, it can also introduce overlay issues as shown in Figure Figure 2.2 [24, 25]. Most of the problems of LELE are solved by using a SADP patterning process.

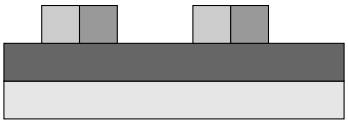

Figure 2.2: LELE overlay issues for a 1:1 features, following step 3 in Figure 2.1

2.1.2 Self-Aligned Double Patterning

SADP is also a lithography based process by which a pattern is made over multiple steps that introduces new deposition and etch related issues affecting the line:space ratio not found in LELE, but none of the overlay issues. SADP does require a second cut or block mask to clean up the final image when the process is complete in most circumstances. The SADP process starts by patterning a mandrel as depicted by the top level of Figure 2.3 forming the primary pattern. The mandrel is then trimmed through

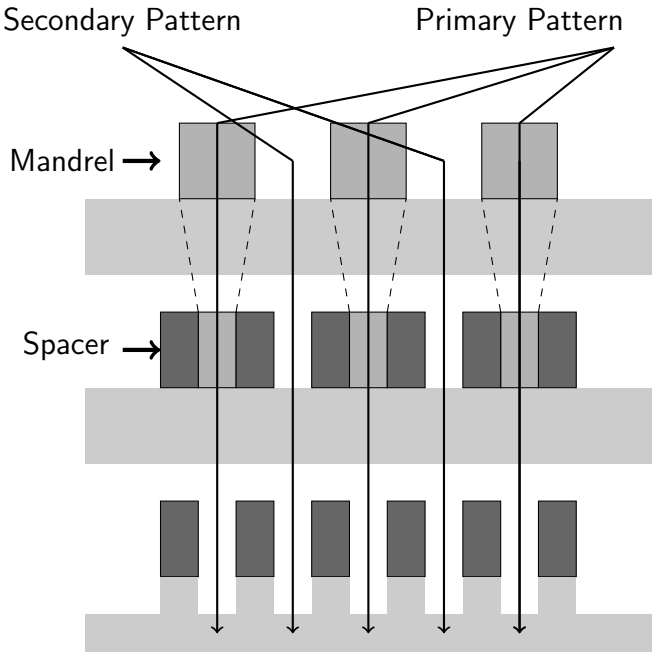

Figure 2.3: SADP simplified flow [26]

means of over-development or overetch and a different film is deposited over and etched back forming spacers on the sidewalls of the mandrel. The mandrel then gets stripped leaving the two sidewalls behind in ideally a 1:1 line:space ratio with the original spaces

being defined as the secondary pattern [26]. Then a cut or trim mask can be used to clean up the features as depicted in Figure 2.4. This is a required step as the spacers are formed around the mandrel and may produce some artifacts that need to be removed in order for shorts or other defects to not occur [24, 26]. As features have gotten smaller SADP has been used in conjunction with a-carbon or newer SOC materials to incorporate etch stops as well as hardmask/BARC layers into the process. The incorporation of these newer materials has also removed the majority of standing wave effects in resist as a problem during subsequent etch processes [24, 26–31]. Additionally the use of dry plasma processing as opposed to wet chemical etching improved the resulting patterned profile.

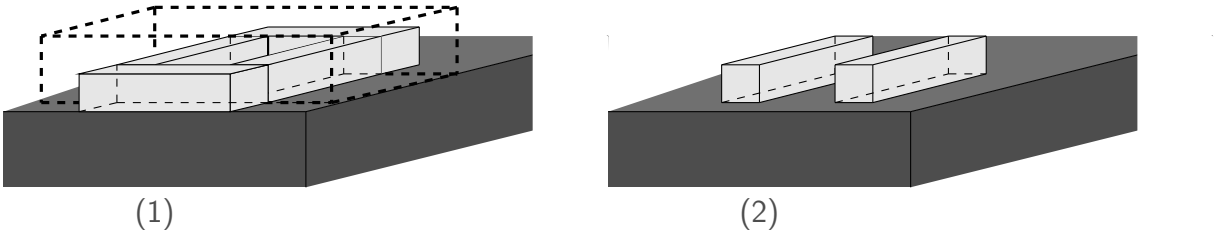

Figure 2.4: SADP cut mask before(1) and after(2) [26].

2.2 Plasma Processing

Plasma processing has had a long history within the semiconductor industry in both coating and etching materials. In plasma processing whether depositing or etching the primary mechanisms are the same. The various types of coating and etching that are used within industry are depicted in Figure 2.5. What isn't listed is that ion implantation is a plasma process similar to Ion Beam Coating (IBC). The most common processes are Plasma-Enhanced Chemical Vapor Deposition (PECVD) and sputtering for coating. The primary focus here is on glow discharge plasmas, specifically for PECVD and Reactive Ion Etch (RIE). A glow discharge plasma is created by inducing an electric field between an anode and a cathode within a vacuum. This can be done with DC current or RF modulated

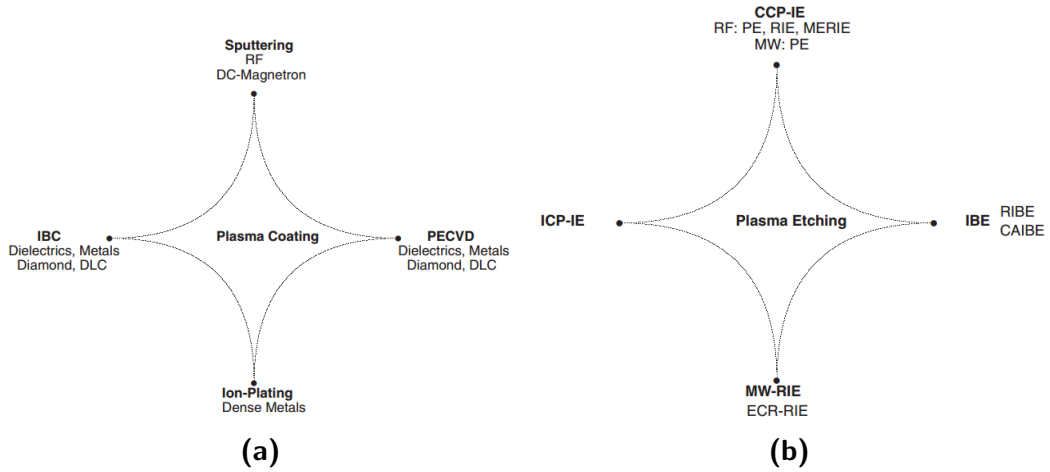

Figure 2.5: Types of plasma coating(a) and etching(b) technology [32].

current also known as a Capacitively Coupled Plasma (CCP). All of this is done to achieve the proper current density in the normal glow region of $10^{-5} \rightarrow 10^{-3} A/cm^2$ as shown in Figure 2.6. To start the plasma, an electric field between an anode and cathode of

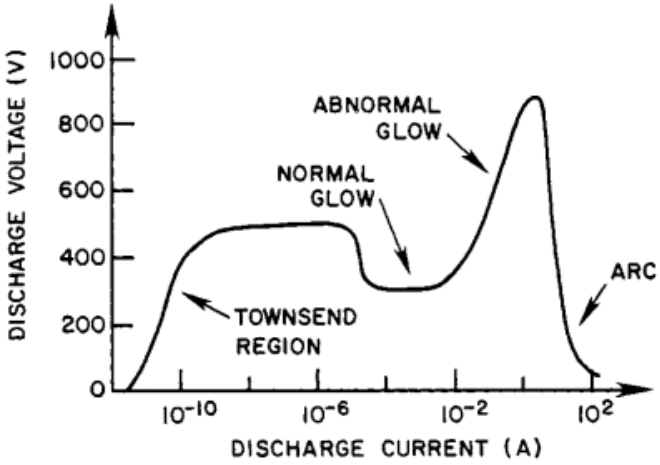

Figure 2.6: Current-Voltage relation for plasma activation [33]

distance d is induced in the chamber, where the field is measured simply as V/d. The electrons present accelerate towards the anode ionizing a gaseous atom and producing another electron in the process. This ion then accelerates towards the cathode due to the induced electric field [33, 34]. If the ion strikes the cathode at sufficient energy a secondary electron may be emitted(Figure 2.7(7)).

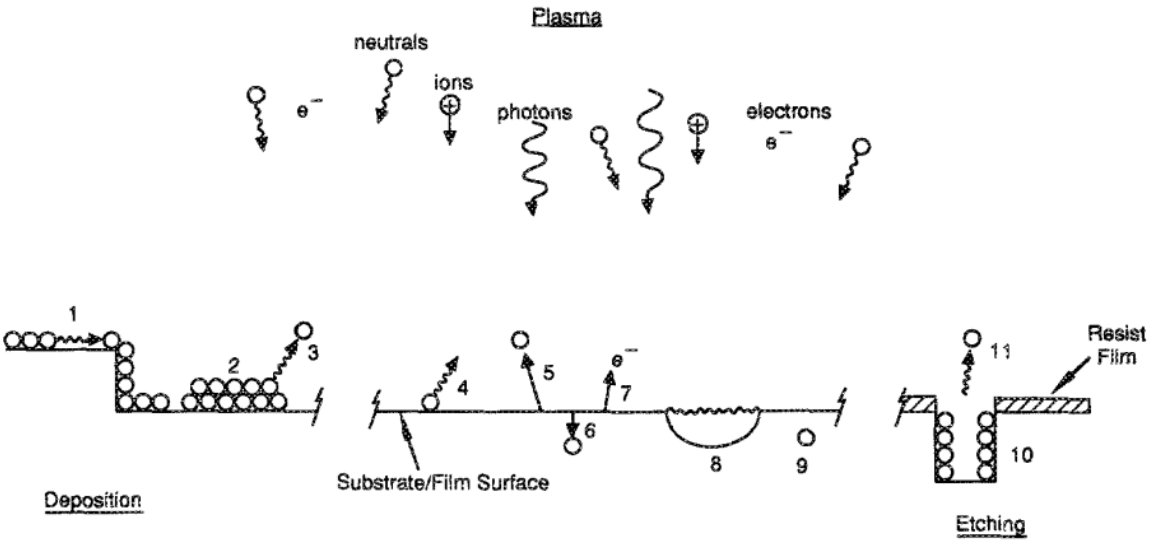

Figure 2.7: Plasma reaction mechanisms [35]

It then follows that continued collisions produce further collisions eventually resulting in a breakdown voltage, also shown as sheath voltage, as shown in Equation 2.1c, where p is pressure in Torr, d is some distance in cm depicting the plasma sheath edge, γ_{se} is the secondary electron emission coefficient, and A, B and C represent experimentally derived constants for a particular gas. The current going to the anode is shown as Equation 2.1a, where α is taken to be the Townsend coefficient shown in Equation 2.1b, and λ_e is the mean free path length for inelastic(ionization) electron-neutral collisions, E is the induced electric field, and $\boldsymbol{V_i}$ is the ionization potential for the gas species. The breakdown voltage shown in Equation 2.1c can be plotted as a function of the pressure and distance to produce what is known as a Paschen curve($\boldsymbol{V_b}(pd)$) whose minima is $\boldsymbol{V_{min}}$ as depicted by Figure 2.8.

$$I_c \exp(\alpha x) = I \tag{2.1a}$$

$$\alpha = \frac{1}{\lambda_e} \exp\left(\frac{\boldsymbol{V_i}}{eE\lambda_e}\right) \equiv pA \exp\left(-\frac{Bp}{E}\right) \tag{2.1b}$$

$$\frac{A(pd)}{C + \ln(pd)} \approxeq \boldsymbol{V_b} = \frac{Bpd}{\ln Apd - \ln[\ln(1 + 1/\gamma_{se})]} \tag{2.1c}$$

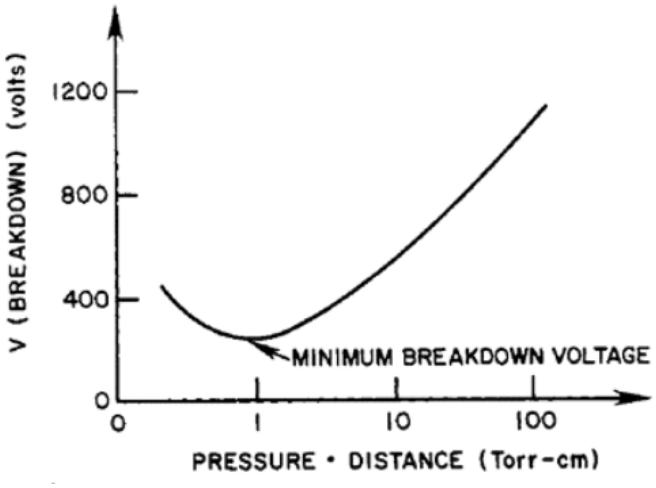

Figure 2.8: A example Paschen Curve depicting the breakdown voltage of a gas between two electrodes separated by a distance d at a pressure p [33]

A Paschen curve exists for every different gas species and cross-section ionization [33, 34]. Before the breakdown voltage is achieved the plasma is in the Townsend region(below $8 * 10^{-5} A/cm^2 = I_A$) once the breakdown voltage is reached a plasma is said to have ignited and be in the normal glow discharge state, also resulting in a drop in overall voltage as depicted by Figure 2.6. As the discharge increases there is a change from the normal glow to abnormal glow used for processing within the cathode sheath [33, 34]. After the plasma is ignited and stable it follows that there is a standard set of chemical reactions that occur, these are shown by Reactions 2.2a through 2.2i, all of which depict both the deposition and etching mechanisms, as shown in Figure 2.7 [34–36].

$$Electron - Ion\ Pair\ Production: \ e + AB \rightarrow AB^+ + 2e \tag{2.2a}$$

$$Radical\ Production: \ e + AB \rightarrow e + A + B \tag{2.2b}$$

$$Negitive\ Ion\ Production: e + AB \rightarrow A^- + B \tag{2.2c}$$

$$Electron\ Affinity: \ A(g) + e \rightarrow A^-(g) \tag{2.2d}$$

$$Gas - Phase\ Reaction: \ A + B \rightarrow C + D \tag{2.2e}$$

$$Ion\ Transport\ flux\ to\ surface:\ \Gamma_i = -D_a \nabla n_i \tag{2.2f}$$

$$Radical\ Transport\ flux\ to\ surface:\ \Gamma_A = -D_A \nabla n_A \tag{2.2g}$$

$$Surface\ Reaction:\ A(g) + B(s) \rightarrow C(g) \tag{2.2h}$$

$$Ionization\ Reaction:\ A(g) \rightarrow A^{+}(g) + e \tag{2.2i}$$

Seeing as deposition and etching have their own quirks it is prudent to describe the reactions that are common for both. As noted before electrons interact with the gases within the chamber, this is shown in Reactions 2.2a through 2.2d, being electron-ion pair, radical, negative ion productions and electron affinity respectively. These reactions produce the ions and radicals that proceed towards the substrate, as depicted by the Fluxes 2.2f and 2.2g. Once the atoms reach the surface the Reaction 2.2h occurs with the creation of adsorption sites with the promotion of new gas species as depicted by Figure 2.7(4). The adsorption site at (4) also alters the film sometimes detrimentally inducing damage as shown in Figure 2.7(8). Both (4) and (8) do however promote film adhesion and further reactions as well as desorption. Sputtering as shown in Figure 2.7(5) can remove species that are trapped or have a low vapor pressure as well as smooth surface topography. Ion implantation also occurs under this mechanism as referenced by Figure 2.7(6) which also creates defects such as trapped gas species as in Figure 2.7(9) [35]. All of these reaction processes are manipulated later in this thesis through the use of Chemical Vapor Deposition (CVD) and RIE to achieve the desired features.

2.2.1 Chemical Vapor Deposition

CVD is a process by which a material is deposited by introducing gases into a chamber and producing a chemical reaction. This method of thin film deposition produces a conformal coating as opposed to similar Physical Vapor Deposition (PVD) methods. There are many different types of reactor chamber configurations, most prominent are

the horizontal and single-wafer vertical or pancake reactors as depicted in Figure 2.9. The reaction chamber dictates how uniform the gas flow and transport of reactants and products to the substrate surface.

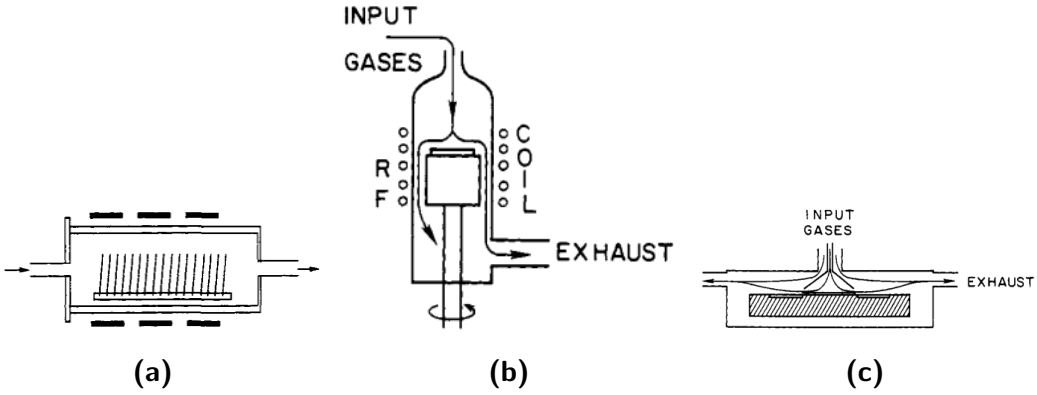

Figure 2.9: CVD horizontal(a), vertical(b), and pancake(c) reaction chambers [33]

All CVD reactions follow a fundamental transport mechanism as depicted in Figure 2.7, replicated here in Figure 2.10, however a plasma is not necessarily required, as higher temperatures are usually used to overcome the ΔU, ΔS and ΔH or internal energy, entropy and enthalpy in the reaction, respectively. In CVD the reaction mechanism is most

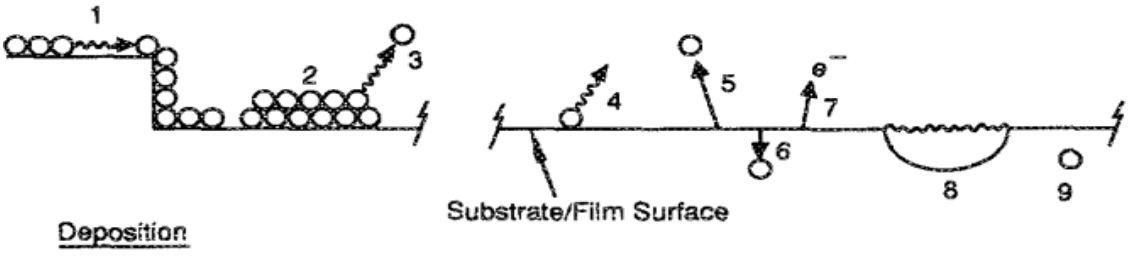

Figure 2.10: Plasma reaction mechanisms, replicated here from Figure 2.7 [35]

commonly seen to be at the sites (1-5) as shown in Figure 2.7. The first step is depicted in Figure 2.7(4) following standard plasma processes, then the atoms are diffused along the surface(Figure 2.7(1)) improving step coverage and altering crystallinity and finding

preferred orientations [33,35,36]. Following surface diffusion comes nucleation and growth where the film densifies as well as rearranges bonds and modifies film stresses. This is best depicted by Figure 2.11, which depicts island, layer and Stranski-Krastanov growth as the primary growth mechanisms. A special note is made for sputtering of the surface(Figure 2.7(5)), for CVD this also improves step coverage and smooths out surface topography in order to achieve a more uniform film. When a plasma is introduced the reaction can proceed forward at lower temperatures than otherwise would be required. To determine whether or not a reaction will proceed forward the Gibbs free energy function(Equation 2.3) is used [36].

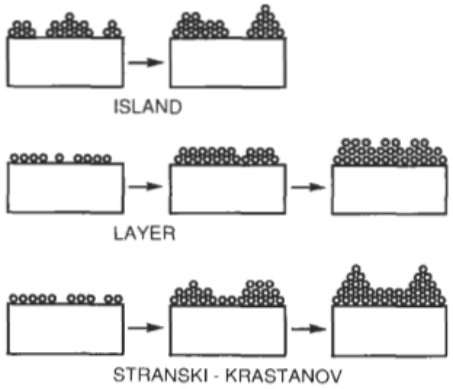

Figure 2.11: Film growth mechanisms [36]

$$\Delta G = \Delta H - T\Delta S \tag{2.3}$$

The Gibbs energy can then be applied to a chemical reaction for each entity within the reaction similar to Equation 2.4 for a simple 3-substance equilibrium reaction, where a, b and c are stoichiometric coefficients. The individual Gibbs energies are depicted by Equation 2.5, where R is the gas constant, G_i^0 is the free energy for a given material in it's normal state, T is the Temperature in K and a_i is a thermodynamic concentration reflecting the change in energy when the substance is not in its normal state. Combining

both Equations 2.4 and 2.5 the Equation 2.6 is produced.

$$\Delta G = cG_C - aG_A - bG_B \tag{2.4}$$

$$G_i = G_i^0 + RT \ln a_i \tag{2.5}$$

$$\Delta G = \Delta G^0 + RT \ln \frac{a_C^c}{a_A^a a_B^b} \tag{2.6}$$

$$\Delta G = RT \ln \left[\frac{\left(a_C / a_{C(eq)}\right)^c}{\left(a_A / a_{A(eq)}\right)^a \left(a_B / a_{B(eq)}\right)^b} \right] \tag{2.7}$$

For the equilibrium state, Equation 2.7 is most useful and one of the most frequently used equations for chemical thermodynamics [36]. The ratio $\left(a_i / a_{i(eq)}\right)$ is a measure of saturation of the species within the reaction, if it exceeds 1, it is supersaturated otherwise under-saturated. This then allows the Gibbs energy to be used as a metric for how the reaction will proceed, most notably in a Gibbs vs temperature curve. Many ΔG^0 by T curves, similar to the example depicted in Figure 2.12, can be invaluable as to the prediction of how a reaction will proceed.

Many other measures of merit exist for how the reaction will proceed, making CVD a very complicated process involving chemistry, physics, gas transport phenomena, as well as thermodynamics. Most notably the Knudsen, Reynolds and Grashof numbers as depicted by Equations 2.8,2.9, and 2.10 are quite useful for determining the feasibility of the reaction [33, 36].

$$Knudsen\ Number:\ Kn = \frac{\lambda}{L} \tag{2.8}$$

$$Reynolds\ Number:\ Re = \frac{\rho v L}{\eta} \tag{2.9}$$

$$Grashof's\ Number:\ Gr_t = \frac{g\rho^2 L^3 \Delta T}{\eta^2 T_t} \tag{2.10}$$

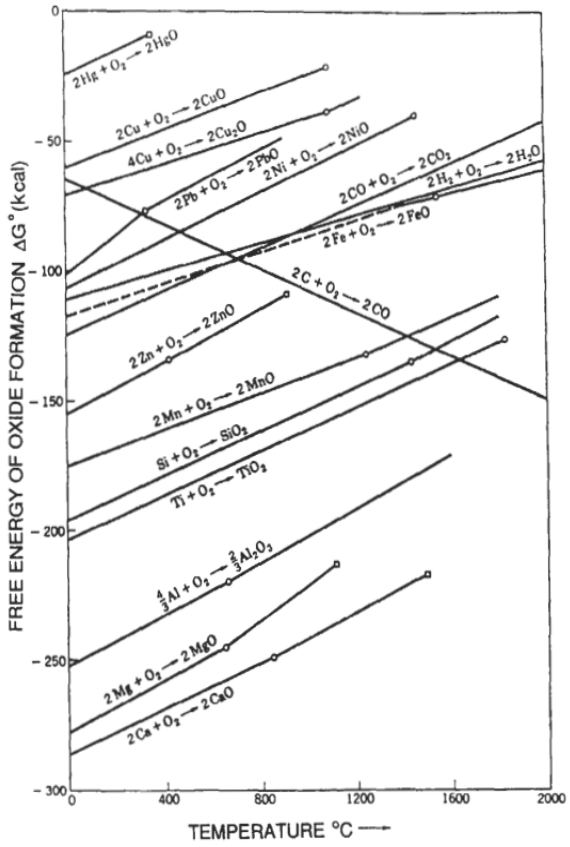

Figure 2.12: A Gibbs energy vs Temperature curve for the formation of various oxides [36].

The Knudsen number is of particular interest as it is the ratio of the mean free path length(λ) and reactor dimension(L). This determines whether or not the majority of the reaction will occur in the continuum or free molecular flow regimes where either gas phase collisions dominate or wall collisions dominate respectively [33]. The Reynolds number depicts the ratio of inertial forces to viscous forces, it is generally used as a indicator of laminar or turbulent flow and has a large impact on temperature distribution within the reaction chamber. The Grashof number gives a representation of the convection within the system with it's ratio of buoyant to viscous forces. The interaction between the Reynolds and Grashof numbers is shown in Figure 2.13.Using these figures of merit a rough idea of how the process will proceed can be obtained.

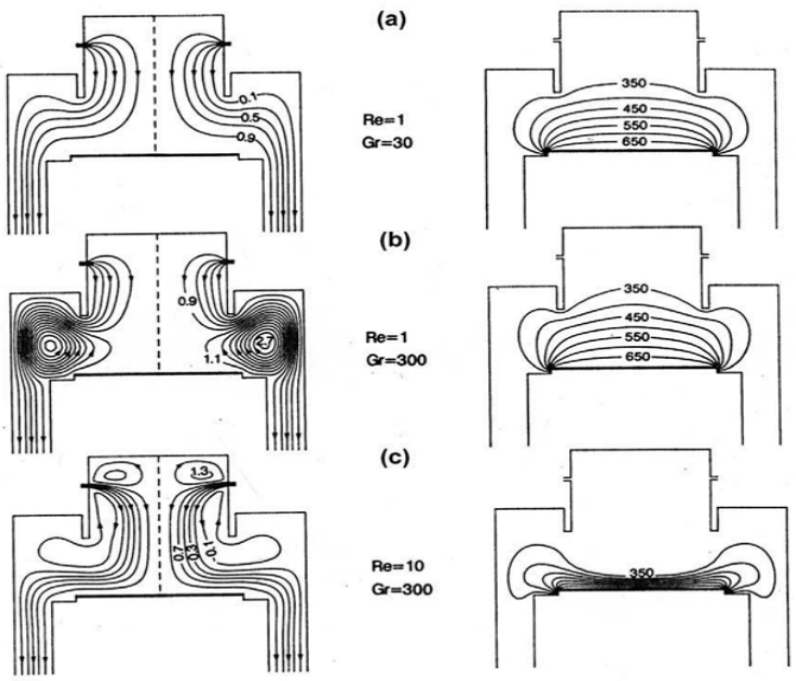

Figure 2.13: Normalized Gas flow lines(left) over the range of 0-1 and isotherms in K(right) for varying Reynolds and Grashof numbers for a vertical reactor design [36, 37].

2.2.1.1 Plasma-Enhanced Chemical Vapor Deposition

PECVD processes follow from standard CVD processes, where additionally a plasma is induced in generally a pancake style reactor(Figure 2.9c) in a cluster type tool with flows similar to that of Figure 2.13. Any standard CVD process has the challenge of conformality to face, whereby a film is placed uniformly from any given surface of the substrate. Deposition tends to occur in a process similar to that depicted in Figure 2.14b, however voids can form as shown in Figure 2.14c. If the film is deposited in a non-conformal matter, the surface of the film is usually has higher surface roughness. Two things usually make a non-conformal surface, either the substrate was rough to begin with or the deposition had incorrect parameters for the film. Generally a conformal deposition is ideal, however many factors allow voids to form as in Figure 2.14. When the precursor mean free path is significantly larger than w or d then ballistic transport takes over producing the deposition shown in Figure 2.14b, which eventually progresses

to Figure 2.14c forming a void or "keyhole" [34]. This metric is distinctly different than uniformity, conformality is important with regards to assuring that patterned features have coverage, whereas uniformity deals with the coverage across the wafer.

One way oxide formation avoids this is not using SiH_4 /O_2 based precursors, and instead using Tetraethyl orthosilicate (TEOS) bubbled through water with the addition of O_2 to the plasma. The reaction tends to follow two examples as depicted by equations

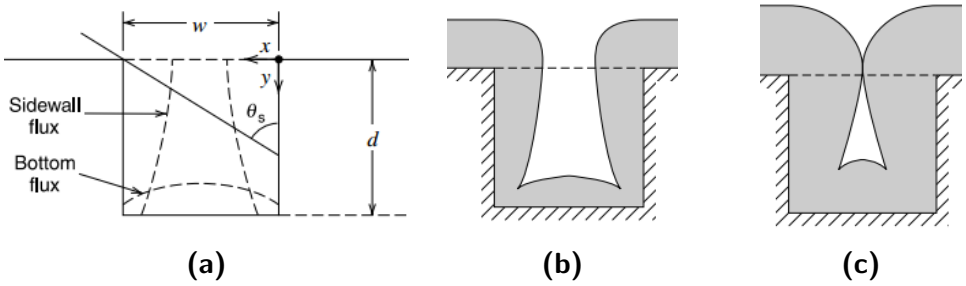

Figure 2.14: CVD formation of voids, w, d is the width and depth of a feature pre-deposition with the incident flux, $\Gamma_{mat} \propto 1 - \cos\theta_s$. [34]

2.11a and 2.11b or that shown in section 2.3.1, Where Reaction 2.11a is defined as electron impact dissociation and Reaction 2.11b is the reactions of the O-atom with the material [34]. In highly dilute reactions 2.11b dominates, producing a more oxide-like film as opposed to a organic-like film provided the TEOS ratio in the gas mixture is roughly 30% as compared to the O_2 flows [34, 38]. This organic-like nature is perceived to be why TEOS films are usually annealed after deposition when the gas mixture is shifted past the 30% mark.

$$e + Si(OC_2H_5)_n(OH)_{4-n} \rightarrow Si(OC_2H_5)_{n-1}(OH)_{4-n+1} + C_2H_4 + e \qquad (2.11a)$$

$$O + Si(OC_2H_5)_n(OH)_{4-n} \rightarrow Si(OC_2H_5)_{n-1}(OH)_{4-n+1} + C_2H_4O \qquad (2.11b)$$

From this the reaction is thought to proceed by having the TEOS precursors connecting to the surface, whereby the number of O atoms(n_{OS}) oxidize producing depo-

sition under the assumption that the reaction rate(D_{SiO_2}) is independent of the precursor for surface coverage and depicted by Equation 2.12a, where the rate constant 0.9 is a fitted parameter [34]. While this is occurring, the O ions also oxidize the TEOS precursor for a deposition rate as shown by Equation 2.12b where u_B is the Bohm velocity or velocity the O ion obtains from the pre-sheath region of the plasma. Some degree of recombination occurs with the O atoms as shown by the recombination flux Equation 2.12c, with the average velocity of the O atom being $\bar{v}_O$, with the increase in temperature producing a logarithmic increase in s_{rec} probability, which decreases n_{OS} reducing overall deposition rate as shown by equation 2.12a [34]. One of the main benefits of PECVD TEOS is it's low temperature process capability, where most depositions for PECVD take place between $200 - 300°C$, under Low-Pressure Chemical Vapor Deposition (LPCVD) conditions for TEOS the temperature range is around $600-800°C$ [33,34]. Under LPCVD the TEOS reaction undergoes pyrolysis(equation 2.13) as opposed to disassociation, at low temperatures H_2 forms instead of water.

$$D^{(1)}_{SiO_2} \approx \frac{0.9 n_{OS}}{n_{SiO_2}} \text{cm s}^{-1} \tag{2.12a}$$

$$D^{(2)}_{SiO_2} \approx \frac{n_{O_2^+} u_B}{n_{SiO_2}} \text{cm s}^{-1} \tag{2.12b}$$

$$\Gamma_{rec} \approx 2 s_{rec}(T) \frac{1}{4} n_{OS} \bar{v}_O \tag{2.12c}$$

$$Si(OC_2H_5)_4 \rightarrow SiO_2 + 4C_2H_4 + 2H_2O \tag{2.13}$$

For silicon nitride depositions silane is still used for PECVD, what changes in the source of nitrogen as opposed to using SiH_2Cl_2 or some derivative as is usually used in LPCVD. For a source of nitrogen, either NH_3 or N_2O are usually used, pure N_2 could also be used as a feedstock. Similarly to TEOS, PECVD silicon nitride depositions occur between $250 - 500°C$ and under LPCVD conditions for TEOS the temperature range is around $750 - 900°C$ [33, 34, 39]. The resulting film can have modified stresses by varying the

electrical properties of the plasma, such as the rf frequency. Interestingly, the source of hydrogen incorporation has been linked to the NH_3 as opposed to the silane, which has led to some use of N_2 as feedstock but at a cost of film quality but does produce a nitrogen-rich film.

2.2.2 Reactive Ion Etching

Similar to PECVD the majority of reactors for Reactive Ion Etch are of the pancake variety(Figure 2.9c). The most common type of RIE reactor is Capacitively Coupled Plasma (CCP) as depicted by Figure 2.15a. Other reactors such as Inductively Coupled Plasma (ICP)(Figure 2.15b) and Electron-Cyclotron Resonance (ECR)(Figure 2.15c) are also becoming more frequently used as higher degrees of control and anisotropy, a metric by which etch directionality is measured, are required. A more thorough treatment of anisotropy is shown in the following section.

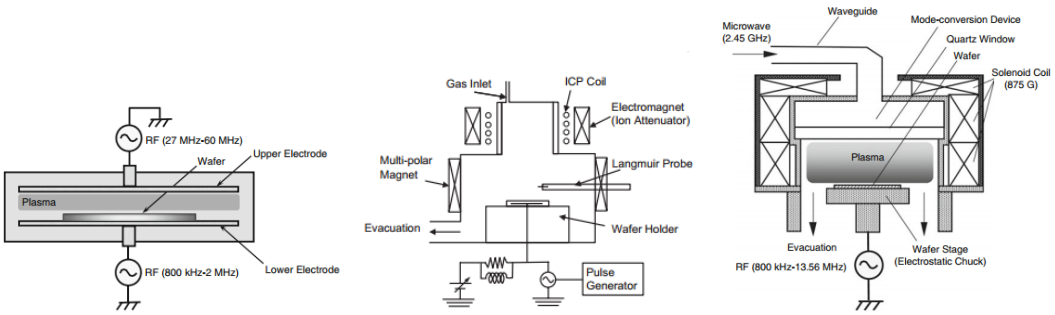

Figure 2.15: RIE Reaction chambers, CCP with low and high frequency RF(a),ICP(b) [40], and ECR(c) [41].

RIE is commonly misused as a term, it is generally associated with the assumption that by introducing the electric field and producing a plasma that the etch is anisotropic, this is simply not the case. The process parameters determine the degree of isotropy not the system itself. In addition the term is a misnomer as neutrals such as

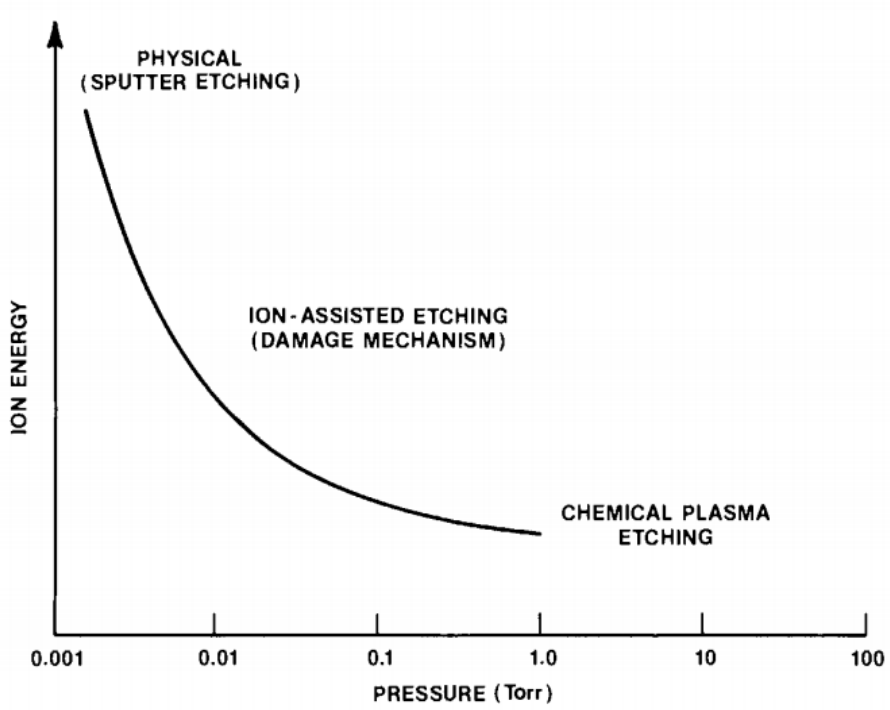

Figure 2.16: Ion bombardment energy by pressure [42].

Fluorine or Oxygen as opposed to ions are the highly reactive species within the plasma. At lower pressures, below 0.01Torr, sputter etching occurs, from 0.01-0.1Torr a mix of sputtering and etching with ions occurs, and above 0.1Torr is closer to chemical plasma etching, this is depicted by Figure 2.16 [42].

In general, feed gases follow the Reactions 2.14a through 2.14g with some examples of gases are shown below [34]. Where, the standard reactions 2.14a to 2.14c represent the majority of reactions, however some films prefer to be etched via unsaturates as in 2.14d. At high pressures or surfaces the reaction depicted by 2.14e can become important. The addition of oxygen or hydrogen as oxidants or reductants either increase the concentration of etchant(2.14f) or remove etchant as volatile products(2.14g) [34].

- Saturates: $CF_4, CCl_4, CF_3Cl, COF_2, SF_6, ...$
- Unsaturates: $CF, CF_2, CF_3, CHF_3, CCl_3, ...$

- Etchants: $F, Cl, Br, O(for\ organics), F_2, Cl_2, Br_2, ...$
- Oxidants: $O, O_2, ...$
- Reductants: $H, H_2, ...$
- Nonreactive Gasses: $Ar, He, ...$

$$e^- + saturate \rightarrow unsaturate + etchant + e^- \tag{2.14a}$$

$$etchant + substrate \rightarrow volitile\ products \tag{2.14b}$$

$$unsaturate + substrate \rightarrow films \tag{2.14c}$$

$$unsaturate + substrate \rightarrow volitile\ products \tag{2.14d}$$

$$etchant + unsaturate(+M) \rightarrow saturate(+M) \tag{2.14e}$$

$$oxidant + unsaturate \rightarrow etchant + volitile\ product \tag{2.14f}$$

$$reductant + etchant \rightarrow volitile\ products \tag{2.14g}$$

The ratio between etchant and unsaturate flux at the substrate balances the isotropy of the etch with film deposition, the key is to form a film in the intermediary between the two finely balanced process. Low F/C feedstock gases(e.g. C_2F_4, C_4F_8) can also be added to reduce the etchant/unsaturate ratio improving sidewall protection while still removing material from the trenches. Inert gases are also added to increase the plasma density, directionality, control the electrical discharge, dilute etchants, substrate thermal properties as well as alter the gas-phase chemistry [34]. For pure F atom etching, equations 2.15a and 2.15b where the density of F-atoms near the surface is n_{FS}, this results in a selectivity of $s \approx 40$ at room temperature(300K) [34]. This shows that under pure F atom chemistry, silicon will tend to etch over oxide.

$$E_{Si}(\text{Å}/\min) = 2.86 * 10^{-12} n_{FS} T^{1/2} e^{-1248/T} \tag{2.15a}$$

$$E_{SiO_2}(\text{Å}/\min) = 0.61 * 10^{-12} n_{FS} T^{1/2} e^{-1892/T} \tag{2.15b}$$

$$s = 4.66 e^{644/T} \tag{2.15c}$$

Generally pure F_2 is not used as a feedstock however as it causes pitting, CF_4 is usually used, as shown to produce the equation 2.16, upon surface reaction.

$$4CF_4 + Si \rightarrow 2C_2F_6 + SiF_4 \tag{2.16}$$

Various papers show characteristics of the CF_4 plasma with respect to oxide,nitride and silicon etching [34, 42–49]. Suffice to say that as a result of this research, the most common etch chemistry used for silicon, oxide and nitride etching is $CHF_3/CF_4/O_2/Ar$ as oxide tends to etch under unsaturate rich conditions, however a more common gas for the etching of silicon and nitrides is SF_6.

Another important metric to look at is the ratio of Power(W) to total Flow(F). This is primarily important to control the deposition of polymer without needing to change the flow ratios and/or their selectivity to materials. If the flow rate is low and the power is high highly carbonated polymer deposits(High W/F). In the opposite situation, high flow and low power, produces a highly fluorinated polymer film, assuming polymer is being deposited in the first place. It also controls the size of said polymer being larger or smaller in particle size [50].

The possible effects of RIE are summarized in Figure 2.17, all of which are dependent on many different aspects of the process and features. A large portion of effects such as undercutting, faceting, bowing, sloped sidewalls, microtrenching and sidewall roughness are primarily due to the effects of the plasma itself, whereas microloading and Aspect Ratio Dependant Etching (ARDE) are mask/feature dependent side effects of RIE, ARDE and microloading are given special attention in Appendix C [34, 42, 51–53].

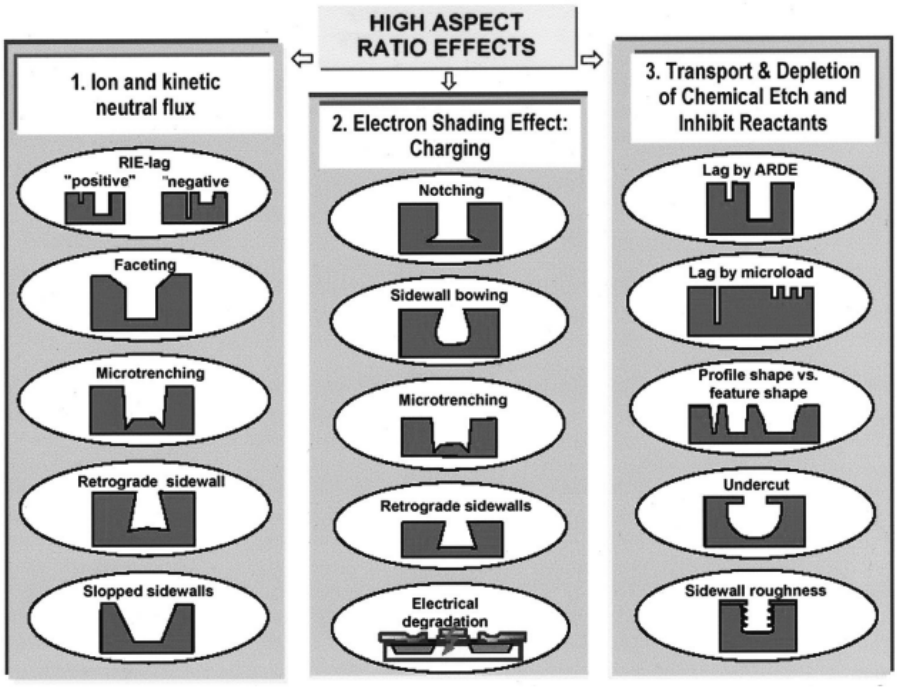

Figure 2.17: Possible effects of RIE [51, 52].

2.2.2.1 Anisotropy, Selectivity and Uniformity

Anisotropy is critical when talking about a RIE process, especially at small scales. There are a large number of factors that affect anisotropy, the pitch, hardmask, hardmask side angle and film selectivity to name a few. The simple equation for anisotropy is shown in Equation 2.17 and its values depicted by Figure 2.18 [42]. The degree of anisotropy is measured by A on a 0 to 1 scale, where 1 is anisotropic and 0 is isotropic in the ideal. The primary component to observe is the etch bias, B, in a purely isotropic etch, the bias will be twice the film thickness. Whereas a purely anisotropic etch will have no horizontal etching, R_h.

$$1 - \frac{|d_m - d_f|}{2y_f} = 1 - \frac{|B|}{2y_f} = A = 1 - \frac{R_h}{R_v} \tag{2.17}$$

Following anisotropy, critical dimensions can then be analyzed as shown in Equation 2.18 [42]. The critical dimension is primarily a function of pitch(d_{Pitch}), final feature

size(d_f), film thickness(y_f) and degree of anisotropy. Through this equation it can be derived that the minimum final feature size can only be twice the film thickness for a given isotropic process for equal line:space pairs.

$$d_c = d_{Pitch} - d_m = d_{Pitch} - |B| - d_f = d_f \left[\frac{d_{Pitch} - d_f}{d_f} - 2(1 - A)\frac{y_f}{d_f} \right] \tag{2.18}$$

Then things start to become complicated, as non-uniformities in the etch, film thickness, and hardmask come into play. The time to clear a film is depicted by equation 2.19 [42]. This incorporates two non-uniformity factors, that of the film(α) and the etch rate(β). This is then followed by the total etch time(2.20 [42]) with the non-uniformity variation of overetching(δ). By contrast, the first time the etched film is broken through is shown by equation 2.21 [42].

$$t_c = \frac{y_f\,[1 + \alpha]}{R_f\,[1 - \beta]} \tag{2.19}$$

$$t_{tot} = t_c(1 + \delta) \tag{2.20}$$

$$t_{min} = \frac{y_f\,[1 - \alpha]}{R_f\,[1 + \beta]} \tag{2.21}$$

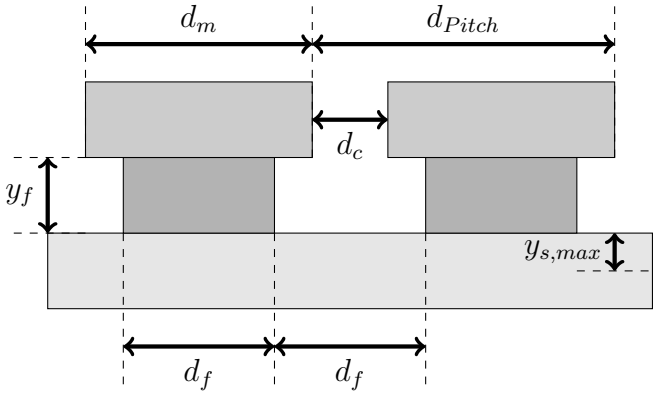

Figure 2.18: Feature size specifications for etching as described by equation 2.18 [42].

All the while, the hardmask is eroding. This erosion is taken to be $\Delta/2$ from

each side of the feature, with an angle θ, where Δ is described by equation 2.22 and depicted by Figure 2.19 [42]. When the total time is expanded the true scope of the non-uniformity factors starts to come to light. This erosion adds yet another non-uniformity factor, ϵ, when selectivity starts to be considered as in equation 2.23 with the uniformity factor being considered in equation 2.24 [42]. Where A_M is the specific anisotropy for the hardmask etch which overall contributes to how much Δ and θ change over time, ignoring the film etch entirely.

$$\Delta = 2t_{tot}(R_h + R_v \cot\theta) = 2\frac{R_v}{R_f} y_f \frac{[1+\alpha]\,[1+\delta]}{[1-\beta]} \left[\cot\theta + \frac{R_h}{R_v}\right] \tag{2.22}$$

$$S_f^m = \frac{y_f}{\Delta} U_f^m \left[\cot\theta + [1 - A_m]\right] \tag{2.23}$$

$$U_f^m = \frac{[1+\alpha]\,[1+\delta]\,[1+\epsilon]}{[1-\beta]} \tag{2.24}$$

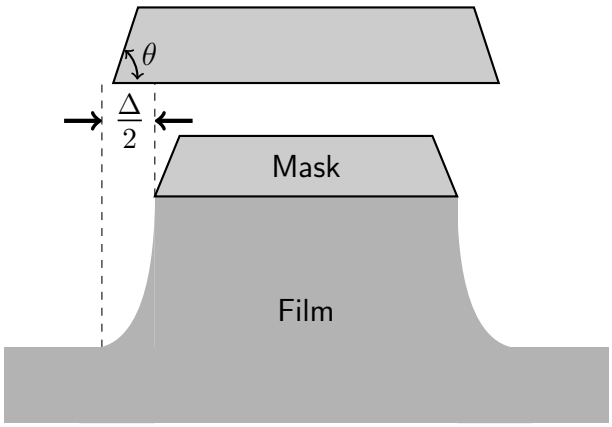

Figure 2.19: Feature shrink due to mask erosion as depicted by equation 2.22 [42].

From all of this then comes the problem of ensuring that while the film clears, there is a maximum depth into the substrate or underlying film($y_{s,max}$) that is allowed for a given erosion rate(R_s) of that material. This is depicted by equation 2.25. Where the corresponding selectivity and uniformity factors follow equations 2.26 and 2.27 respectively [42].

$$y_{s,max} = R_s(t_{tot} - t_{min}) = R_s \frac{y_f}{R_f} \left[\frac{[1+\alpha]\,[1+\delta]}{[1-\beta]} - \frac{[1-\alpha]}{[1+\beta]} \right] \tag{2.25}$$

$$S_s^f = \frac{y_f}{y_{s,max}} U_s^f \tag{2.26}$$

$$U_s^f = \left[\frac{\beta(2+\delta+\alpha\delta) + \alpha(2+\delta) + \delta}{[1-\beta^2]} \right] \tag{2.27}$$

Using all of these factors any given etch, various thicknesses and selectivities can be determined for any range of materials for a given desired feature size.

2.2.2.2 Magnetically Enhanced Reactive Ion Etching

MERIE is a special class of CCP etcher, whereby magnets are placed around the chamber similar to a ECR reactor, here depicted by Figure 2.20. By introducing the magnetic field parallel to the plane of the substrate the particles start to spiral as shown in Figure 2.21.In a MERIE chamber, there are two pairs of magnets just outside the chamber to introduce this field. The introduced field rotates clockwise between the magnets producing a toroid of high-density plasma at the wafer surface. This increase in plasma density helps stabilize and improve directionality and thus the anisotropy of the reactor. It is this field addition that adds further tuning of feature profile to be possible, which is critical for forming the mandrel in this process. [34, 42, 54]

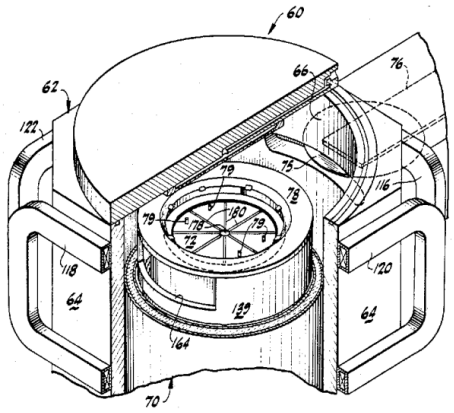

Figure 2.20: MERIE reactor [54, 55]

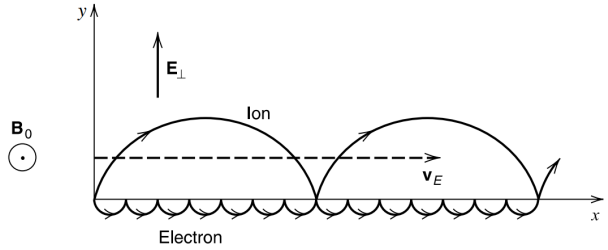

Figure 2.21: The trajectory of electrons and ions in a constant magnetic field [34].

2.3 Spin-On Materials As an Alternative to CVD films

Many materials such as photoresist have been spin coated for a long time, a somewhat newer technology incorporates the same principles and ideas learned from resist to form other spin-on materials. Photoresist materials operate on simple polymer chemistry and physics, other materials however use different mechanisms to achieve a similar goal. In either instance, the materials have various requirements, operate on the process of Chemical Solution Deposition (CSD) and are sensitive to many defects when applied incorrectly. Spin coating has three stages independent of material concern, dispense, flow dominated thinning, solvent evaporation and setting as shown in Figure 2.22. It is recommended that the wafer be spinning during the dispense step as to better facilitate substrate wetting, this at times does require a hydrophobic or hydrophilic surface depending on the material being dispensed, for example HMDS is usually used for

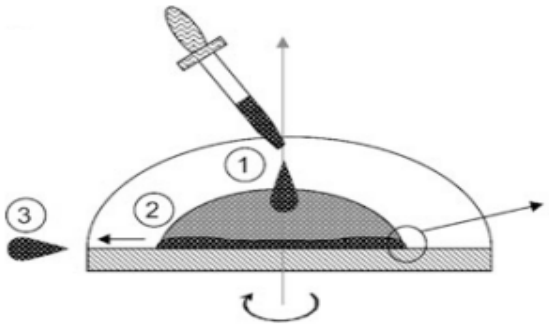

Figure 2.22: The three stages of spin coating: 1:dispense, 2:flow dominated thinning, and 3:solvent evaporation and setting [56]

photoresist surface prep to change the surface from hydrophobic to hydrophilic. Following the dispense of material provided there is good wetting, the material can start to spin out to the desired thickness and undergoes flow dominated thinning as expressed by Figure 2.23. The ramp time for this is usually determined by the manufacturer to achieve the appropriate crossover point at which solvent evaporation can start.It is during this thinning step that a fair portion of the film is deposited around the edge of the substrate forming what is known as the edge bead. Frequently an edge bead removal spin is added after the solvent evaporation phase of deposition.

During the solvent evaporation stage the film starts to densify as a viscous colloidal suspension(sol), semisolid or pre-polymer solution. It is at this state that further processing is performed to start to thermoset the material further driving off more solvent. Spin defects generally arise from too low a dispense volume, too hot of a substrate, inappropriate exhaust, inappropriate chuck material, to high a spin speed, spun material temperature or old material. The two most common defects are comets and striations. Comets arise from particulates in the dispensed liquid sticking to the substrate surface and impeding flow generating an expanding cone of streaking towards the radial edge. Striations are formed due to capillary action that becomes unbalanced due to surface tension differences along the substrate, best described through Figure 2.24.

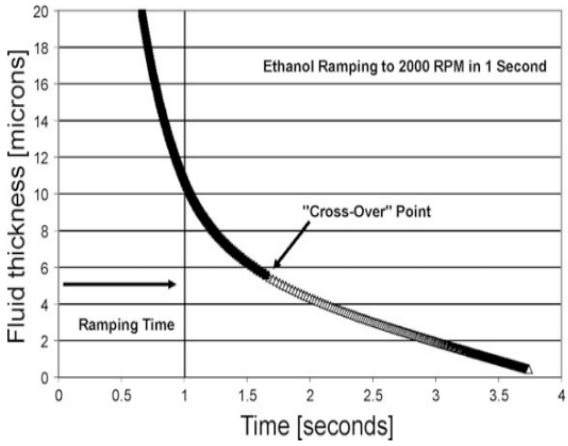

Figure 2.23: Solvent thinning following the material dispense. At the "cross-over" point the material stops undergoing flow dominated thinning and enters the solvent evaporation stage. [56]

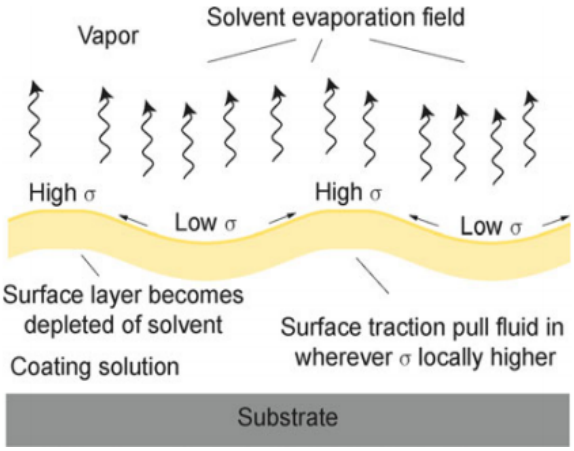

Figure 2.24: The solvent evaporation stage with respect to surface morphology. [56]

2.3.1 Spin-On Glass

SOG materials form on average from a sol-gel process. This process involves a single-phase solution/sol that transitions from the liquid phase to the solid phase forming a two-phase gel consisting of solid and solvent filled pores. The transition occurs via destabilization, precipitation or supersaturation. The standard example follows the formation of silicon dioxide via the Stöber process for hydrolyzing TEOS, to which a simplified diagram is shown in Figure 2.25. When TEOS($Si(OC_2H_5)_4$) is dissolved in ethanol or other organic solvent it allows it to react with water in solution. The Process follows

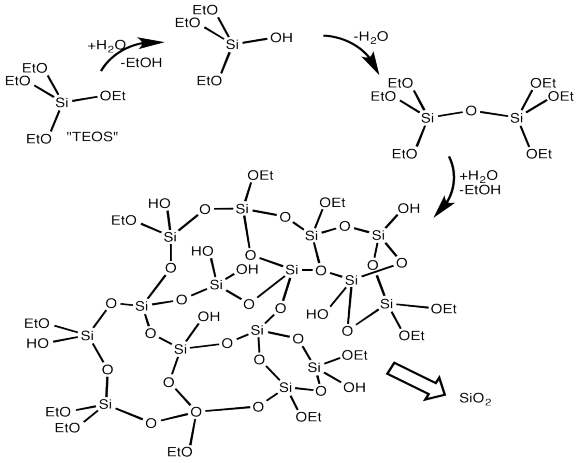

Figure 2.25: Sol-Gel/Stöber Process for TEOS [57]

a couple different reactions, listed below(2.28) in order to form an oxide film. The first two reactions 2.28a and 2.28b hydrolyze the TEOS forming a silanol product. The other three reactions, 2.28c,2.28d and 2.28e all take the silanol product and start the process of polymerization, where in the case of reactions 2.28c and 2.28e more water is produced for further hydrolysis [33].

$$Si(OC_2H_5)_4 + H_2O \rightarrow Si(OC_2H_5)_3OH + C_2H_5OH \quad (2.28a)$$

$$Si(OC_2H_5)_4 + 2H_2O \rightarrow Si(OC_2H_5)_2(OH)_2 + (C_2H_5OH)_2 \quad (2.28b)$$

$$2Si(OC_2H_5)_3OH \rightarrow (C_2H_5O)_3Si - O - Si(OC_2H_5O)_3 + H_2O \quad (2.28c)$$

$$Si(OC_2H_5)_3OH + Si(OC_2H_5)_4 \rightarrow (C_2H_5O)_3Si - O - Si(OC_2H_5O)_3 + C_2H_5OH \quad (2.28d)$$

$$Si(OC_2H_5)_3OH + Si(OC_2H_5)_2(OH)_2 \rightarrow (C_2H_5O)_3Si - O - Si((OC_2H_5O)_3)_2OH + H_2O \quad (2.28e)$$

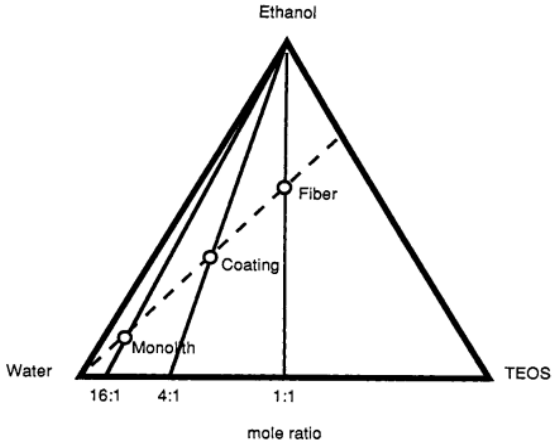

Figure 2.26: The TEOS-ethanol-water system for sol-gel depositions [33].

Following the TEOS example, when the water to TEOS and ethanol to TEOS ratios are equal, as shown by the dotted line in Figure 2.26, the material can then be formed into a coat-able thin film material. Once the deposited film undergoes the final cross-linking completing the sol-gel transition, the solvent phase (ethanol in TEOS and stage 3 in a spin coat process) is removed, and the material is then considered a gel. Often times the gel still contains solvent that must be removed further to completely dry the coating forming the true microporous oxide film [33, 58]. As films progressed SOG became a spin on dopant material as well as a planarization material by varying what the feedstock sol-gel precursor was, with it usually being some form of TEOS-derived material.

2.3.2 Spin-On Carbon

Carbon has been used in industry as a hardmask for a while, especially at the beginning of the start of double patterning. The first hardmasks were using a diamond-like amorphous carbon, chosen due to its high selectivity to any number of standard CMOS materials. [27, 29, 59–61] To call the material used diamond-like is a bit of a misnomer as the material that was generated via a CVD process generally resided within the ta-C:H and a-C:H regions of the ternary phase diagram as depicted by Figure 2.27. As features got smaller the a-carbon materials became too thick and changes needed to be made [62], so carbon based spin-on materials were developed. Initially there were some troubles producing a comparable material to the a-carbon [63, 64], namely with concerns to wiggling [65, 66]. These problems started to go away when the fullerene material

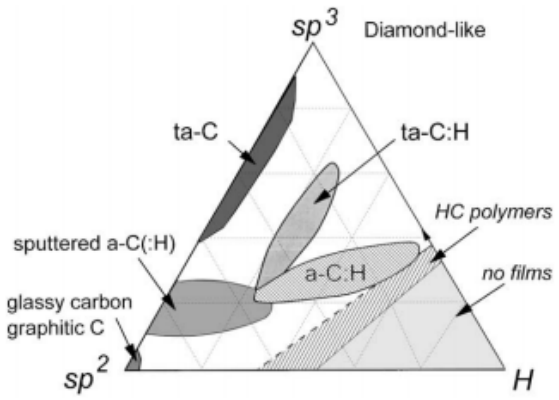

Figure 2.27: Carbon ternary phase diagram [67, 68].

was developed [66, 69, 70]. The fullerene based material "IM-HM-140" from Irresistible Materials(IM) [71] used here is similar to resist in that it had a Novalac based epoxy resin for its crosslinking material as shown in Figure 2.28b, with the fullerene based monomer being shown in Figure 2.28a. The material developed by IM [71], is different than some of the initial fullerene based hardmasks [69, 70] but shows good etching characteristics for deep etching [66, 71, 72]. It has also been shown that multi-layer resist stacks perform well for both a BARC as well as a hardmask for patterning [21, 27, 29, 59–61, 73].

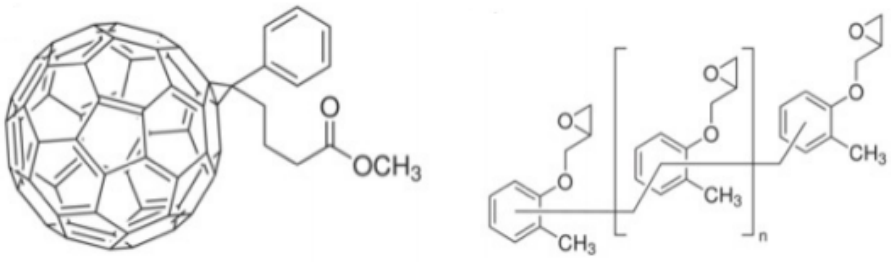

(a) **(b)**

Figure 2.28: Polymer precursors of the "IM-HM-140" SOC material. A fullerene based monomer(Phenyl C60 Butyric Acid Methyl Ester) is shown in (a), which is also used in organic polymer based electronics as an acceptor [74], and standard Novolac crosslinking material(Poly[(o-cresyl glycidyl ether)-coformaldehyde]) is shown in (b) [66].

Process Flow and Experimental Investigation

The process flow developed at RIT was designed to closely reproduce what the semiconductor industry uses for a SADP process module while advancing what RIT's current cleanroom facilities are capable of [24, 26–31]. This chapter is broken up into two sections, the proposed process flow for a complete FinFET etch module as well as an experiment to ensure that the films are etched with proper rate, selectivity and anisotropy. The etching experiment is proposed such that a high degree of etch control can be achieved with the MERIE system that RIT, which does not have an spectrophotometer for endpoint detection. Without the proper etch data a number of critical steps, namely the etch processes described within sections 3.1.6 and 3.1.9, would be incredibly difficult.

3.1 Process flow

The SADP process outlined here is a first step in FinFET fin formation and is referred to in an idealized context throughout, predominantly perfect selectivity and uniformity are assumed. This process could be expanded to quadruple patterning by simply adding two additional layers, and will be noted when applicable for a conversion of this process into a quadruple patterning process. All drawings are rough depictions to illustrate the challenges posed, in each step any nuances not depicted are described. It is

worth noting that this process has a significant throughput improvement over other RIT SADP processes in that the entirety of the process can be contained within a cluster tool consisting of a MERIE etcher, PECVD TEOS oxide and PECVD nitride chambers [19].

3.1.1 SOC Fin Hardmask Deposition

The selection of hardmask for etching silicon generally is not particularly important as both common oxides and nitrides are fairly selective to silicon with oxide alone having standard ratios of 4:1 to 25:1 depending on the reference. These etch rates are generally quoted for wet chemical etching however as opposed to dry etching [42]. A very high selectivity is required for a high aspect ratio etch of at least 1:3 hardmask:substrate is required. This is where carbon hardmasks have come into play and why a fullerene derived-SOC was chosen for this layer. In addition to its selectivity to SiO_2, Si_3N_4, and Si. Previous work at RIT has demonstrated the SOC to be a good hardmask material with high-aspect ratio silicon etches [21].

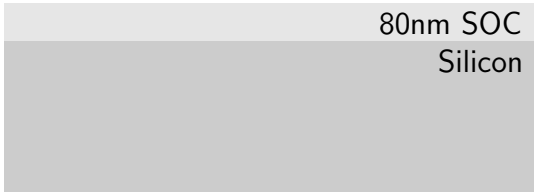

Figure 3.1: Deposition of the first SOC layer

3.1.2 Oxide Mandrel Deposition

The next layer to be considered is the mandrel over which the spacers are formed. This could be chosen to be a variety of things but is most commonly either a nitride or oxide. Here a PECVD TEOS oxide was chosen to be the mandrel material. 120nm of oxide is the chosen thickness for this process as 100nm is the designed critical dimension, the 20nm is intended for overetch as discussed in 3.1.6. If this process were to be expanded

to be a quadruple patterning process, a PECVD nitride and SOC layer would be added beneath these two layers in a similar fashion with the SOC on the bottom.

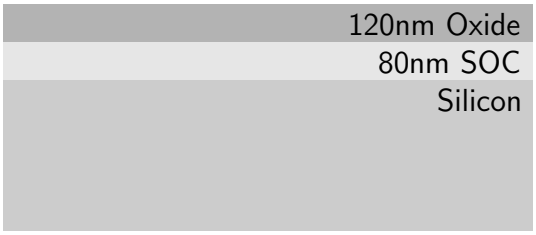

Figure 3.2: Deposition of what will be the mandrel layer out of PECVD TEOS oxide

3.1.3 BARC Deposition

With this process the goal is to achieve sub-lithographic features, as such a Bottom Anti-Reflective Coating(BARC) should be deposited below the resist layer. Previous work has used a SOG over SOC in order to use the SOC as a hardmask for the oxide etch [19, 21]. The SOG was investigated(see Section 4.1) and determined to be a poor material for this project and with etch process improvements the SOC might not be necessary. If the etch process is not as anisotropic with high enough selectivity, a layer of SOC could be added prior to the BARC and very minor changes would be required. The BARC thickness has previously been determined to be 65nm for good performance.

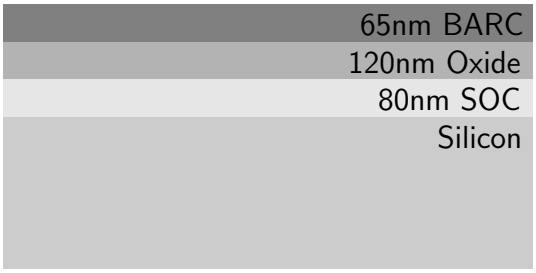

Figure 3.3: Deposition of the BARC layer

3.1.4 Resist Coat, Expose and Develop

Photoresist is then coated onto the film stack as shown in Figure 3.4a. The photoresist is then exposed as depicted in Figure 3.4b and developed as shown in Figure 3.4c. If the photoresist is over-exposed or over-developed a thinner resist image is what results. Maintaining good critical dimension over the whole wafer in this regime using the chemical development process is tricky. As such going forward a trim etch was chosen using higher image quality from normal exposure/develop steps.

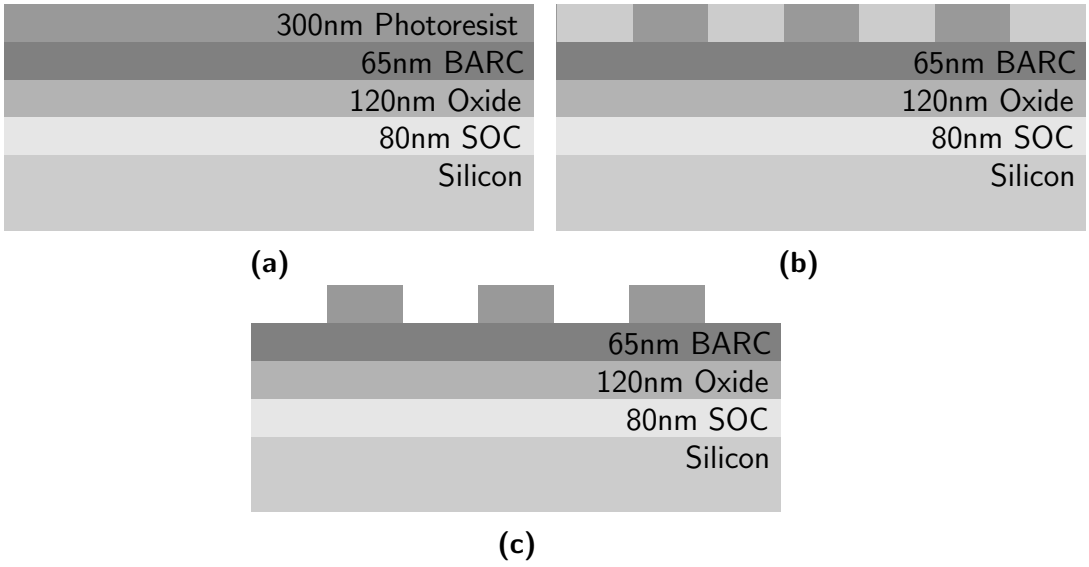

Figure 3.4: Photoresist coat of the film stack(a) followed by the exposure of the mandrel layer pattern(b) and the development of the Mandrel layer pattern(c)

3.1.5 BARC Open and Trim Etch

The BARC open etch is required as the BARC layer does not develop with the resist. This is preformed with a O_2 etch. Following the BARC etch/open as shown in Figure 3.5a, the next step is to trim the pattern for the mandrel define etch that follows as shown in Figure 3.5b. The trim etch is effectively a controlled overetch of the BARC with a slow known rate for critical dimension definition.

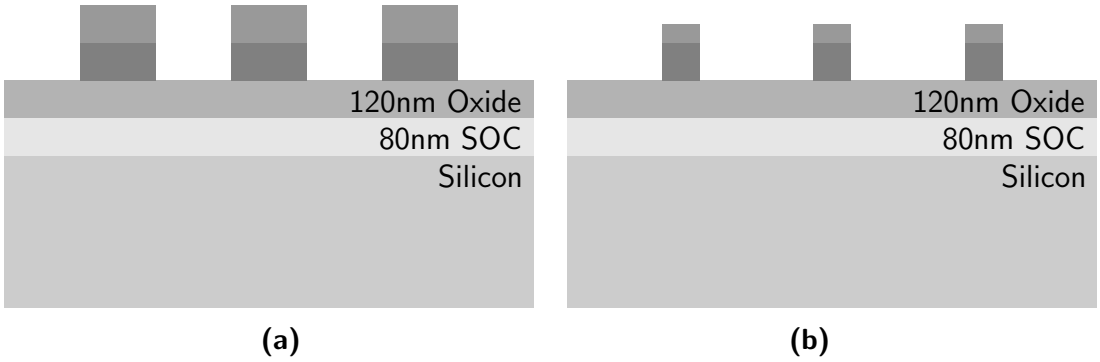

Figure 3.5: The BARC open etch opens up the BARC layer as shown in (a). Then the etch continues producing a trimmed feature with the trim etch as depicted in (b)

3.1.6 Mandrel Etch

This step is absolutely critical while also complicated. The primary etch gasses for a SiO_2 etch are CF_4 and CHF_3 . The etch needs to be as perfectly anisotropic as possible for critical dimension definition for the sidewall spacers that come next. What makes it complicated is that the BARC must be removed prior to the deposition of the sidewall spacers. The BARC strip cannot be performed after the mandrel etch completes as the SOC fin hardmask is exposed and etches in the same strip chemistry(O_2 plasma). So, what needs to be done is to stop the mandrel etch short as shown in Figure 3.6a. The top TEOS layer should also be deposited/etched sufficiently during previous processing/trimming such that it is fully removed prior to stopping the mandrel etch short. Then as depicted by Figure 3.6b the BARC layer can be stripped allowing for the completion of the etch in Figure 3.6c.

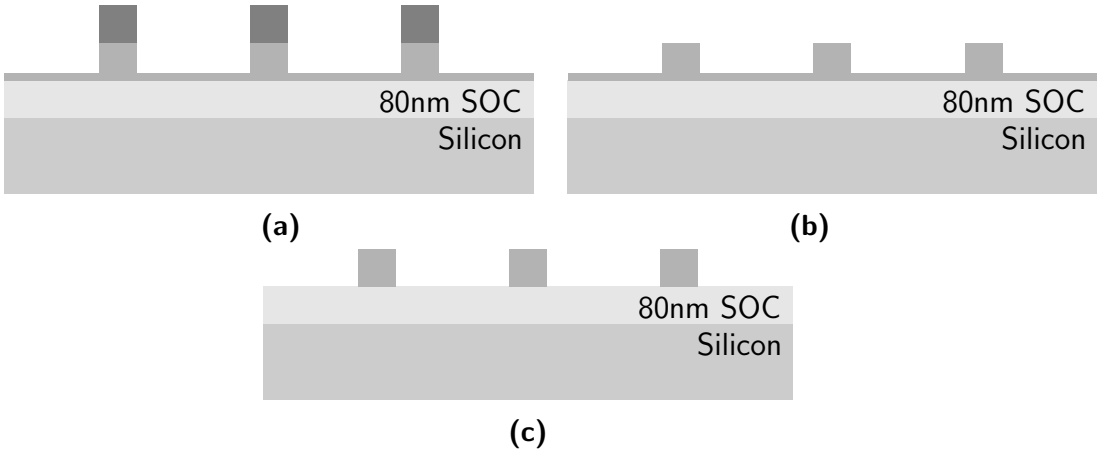

Figure 3.6: There are three steps to the mandrel etch. (a) shows the initial etch stopping short, followed by a strip of the SOC hardmask in (b) and finally completing the etch in (c)

3.1.7 PECVD Nitride Deposition

The nitride deposition for this step has a fair number of factors involved as well. PECVD was chosen over LPCVD for a number of reasons, one simply is convenience and efficiency; the PECVD Nitride chamber that RIT possesses is housed within the same cluster tool that the MERIE dry etch chamber is so the wafers need only to move from one chamber to another. In addition, PECVD takes significantly less time(minutes as opposed to hours) as opposed to LPCVD and is likely more conformal partly based on previous work [19]. Also, due to the SOC the process cannot use the LPCVD as the temperatures for deposition are around $800°C$ as opposed to PECVD which is around $400°C$, at around $300 - 400°C$ the SOC starts to erode at 12nm min^{-1}. This temperature constraint for the SOC is a primary driving force for using PECVD as opposed to LPCVD as in the LPCVD the SOC would erode completely before the deposition would even occur. The amount deposited should match very closely to the total height of the mandrel for the following spacer etch step as this deposition does come to define a good portion of the critical dimension for the spacers.

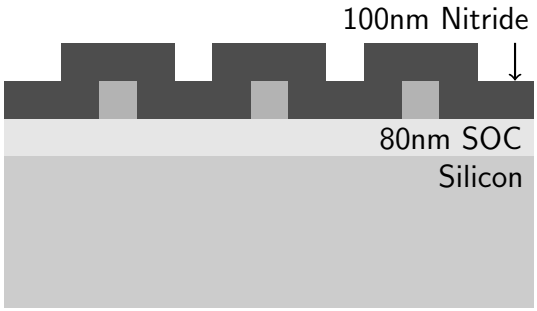

Figure 3.7: Deposition of the nitride spacer layer

3.1.8 Nitride Spacer Etch

For the spacer etch things become difficult, the nitride film when deposited at the thickness of the mandrel has double the thickness where the spacer is to be. This doubling of thickness allows for a bit of process variability, the etch should be performed such that the etch is as uniform as possible under predominantly vertical etching.

Figure 3.8: Etching of the nitride spacer layer

3.1.9 Mandrel Strip

The mandrel strip step is a key point in this process as a dry etch under the conditions within RIT's MERIE chamber. Both the mandrel and the spacer films need to be carefully calibrated such that selectivity is high under the chemistry(CF_4 /CHF_3 /C_2F_6) in the MERIE chamber. Under these chemistries the selectivity is normally 1:1 or predominantly etches the nitride faster, despite polymer film forming thicker on nitrides as opposed to oxides during normal etching [34, 42, 75]. An improvement in selectivity

has been found but requires more research by determining an optimal etch, modifying the material chemistry, and/or performing a pseudo-Bosch etch. The Bosch etch would consist of a step-wise process of depositing just enough polymer for the following etch step to only break through the oxide polymer then repeat the process, until the oxide is stripped. This is different from a standard Bosch etch in that it involves multiple materials as well as a anisotropic etch is performed as opposed to an isotropic etch that does not etch where the polymer was deposited [41, 76–78].

Figure 3.9: Removal of the oxide mandrel

3.1.10 SOC etch

After the mandrel is stripped the nitride spacer can be used as a hard mask to etch the bottom SOC in final preparation for the fin etch. It is at this point that the nitride spacer could also be stripped, however there is little need as the nitride layer will likely erode during the fin etch.

Figure 3.10: Etch of the SOC hardmask for the fin etch

3.1.11 Silicon Fin Etch

With the final pattern established the fin etch can finally be performed. SOC was chosen to be the final hard mask as a fair amount of etch chemistry that etches silicon will also etch nitride, so a 1:3 horizontal:vertical etch profile would be very hard due to mask erosion. A 1:3 profile is required to adequately call the feature a fin. From this point, or during the etch itself, the fin can be tapered for better electrical properties.

Figure 3.11: Final fin etch into silicon substrate

3.2 Etch Rate, Anisotropy and Selectivity Study of Oxide Etching

In order to have a controllable etch that is precise there are five key components; the etch rate, anisotropy and selectivity of the hardmask, the material to be patterned as well as the underlying material beneath it. Uniformity is looked at after selectivity is achieved. Without endpoint detection the mandrel etch(Section 3.1.6) and mandrel strip(Section 3.1.9) are especially difficult. To begin to determine these response factors a screening etch was developed as shown in Table 3.1.

RIT's standard P5000 MERIE oxide etch recipe(B.1) has O_2 as part of the process introduced to quell polymer buildup. In this experiment O_2 was not selected to be used as O_2 is more important once a it is determined how much polymer is formed and whether or not it is excessive. The addition of O_2 also changes selectivity to carbon-based films as O_2 is the primary etchant in that material system, which provides further reason to not include it in testing as the materials for the test listed as follows: Si, Si_3N_4,

SiO_2, SiO_xF_y, photoresist, and SOC. BARC was not chosen as a material as in general it has a similar rate to photoresist and since photoresist is already a film in the test it would be redundant. The primary inputs are the three etch gases; CHF_3 ,CF_4 and C_2F_6 , varied over five levels;0,15,30,45,and 60. Power, Pressure, Magnetic Field are held constant throughout the test as they modify the rate and profile in more predictive ways while not affecting the selectivity. Ar is also held constant as it provides directionality by breaking through inhibitor formation in inhibitor-driven anisotropic ion enhanced etching, even though it does change the partial pressures of the etches.

Through cross-sectional analysis, both vertical(R_v) and horizontal(R_h) etch rates could be determined to show how anisotropic(A) the etch was and if the etch would be within the acceptable tolerances for the given etch per Equation 2.17. Mask erosion rates would be determined through Equation 2.22. For uniformity(Equations 2.24 and 2.27) the constants, α, ϵ, and δ are predominantly determined from how much the film to be etched is uniform, erosion/how uniform the hardmask is and overetch is acceptable/required for the process. β however will be determined through running the process with blanket oxide over 6" wafers as the uniformity variance in the etch has more to do with the conditions of the etch process as opposed to the film itself.

Test	CHF_3 (SCCM)	CF_4 (SCCM)	C_2F_6 (SCCM)	Sample
1	0	0	45	a
2	0	30	30	b
3	0	60	60	c
4	15	15	30	d
5	15	30	15	e
6	15	45	45	f
7	30	0	60	g
8	30	30	0	h
9	30	45	15	i
10	45	0	30	j
11	45	15	0	k
12	45	60	45	m
13	60	15	60	n
14	60	45	0	p
15	60	60	15	q

Table 3.1: Enchant selectivity test
Power:500W, Pressure:250mTorr, Magnetic Field:60G, Ar :100 SCCM

Film Uniformity and Etching

4.1 SOG and TEOS uniformity

For various stages in the process, uniform film deposition is important either for better coverage or for reducing the time spent overetching to clear the entire wafer. Since PECVD Nitride was unavailable at the time of this study a focus was placed on the use of SOG and TEOS. There were numerous issues with the SOG that RIT has, one major issue was that the material was quite old producing comets and streaking as shown in Figure 4.1. The streaking was caused by having too high surface tension from having too large a percentage of TEOS to carrier solvent, ethanol, not allowing the material to flow properly. The SOG was re-diluted in an attempt to remove the streaking but the film was still less uniform than preferred as shown in table 4.1. With 6% non-uniformity and a 100nm range, that is well below the acceptable tolerance for a SADP process.

With the SOG not performing well enough to process with, TEOS provided a good alternative. It can be deposited over the hardbaked SOC for the mandrel layer. RIT's TEOS performed fairly well. A uniformity test was conducted over 26 wafers. Standard processing only permits 1µm of depositions between cleans, so as such, two 5kÅ/500nm depositions were performed and then a clean was run. Before all the depositions, a minimum of 3 hours between the startup of the lamps and the actual deposition was

maintained. This lag time is important as the lamps provide even uniform heating to 390°C throughout the chamber, RIT turns the lamps off at night to conserve power and as a preventive maintenance measure to not replace the bulbs as often as the tool does not see 24/7 use. A trend was shown that the first wafer after a clean was slightly less uniform, on the order of 0.59% or 10nm across the wafer as shown in Table 4.2 through a 81 point scan. With a range of around 20-30nm and non-uniformity from 0.8-1.3%, TEOS produces a viable outlet for a mandrel material over SOC for the proposed process sections 3.1.2-3.1.6. However, a different material may be required to be developed such as a fluorine-doped TEOS better known as Fluorinated silica glass (FSG) or a more organic TEOS film for the mandrel removal step(process section 3.1.9) as the SOC material could be removed if exposed to water as would be the case in a rinse tank following a Buffered Oxide Etch (BOE) [38, 79, 80]. It can be safely assumed that proceeding with the TEOS as is is advised, and would produce a α value of around 0.01 for use in etch calculations.

Figure 4.1: SOG coating depicting streaks and comets

	Before	After
Mean(Å)	8008	4419
Non-uniformity %	15	6
Range(Å)	4857	1216

Table 4.1: Average uniformity of SOG before and after ethanol addition.

	Average	1st	2nd
Mean(Å)	5358	5314	5401
Std dev	55	68	42
%	1	1.3	0.79
Range(Å)	247	298	195

Table 4.2: Average uniformity for 5kÅ depositions as well as the average data for first and second wafer through after a clean.

4.2 TEOS Etching

In order for RIT to achieve small features for a SADP process, a significant focus needs to be placed on etching. Currently RIT has two types of etchers, CCP and a MERIE etcher, Uniformity control on standard CCP etchers is fairly poor so this work focused on the MERIE etcher. However the MERIE etcher was in a bit of disarray, largely, when the tool was donated it was not given a proper cleaning prior to its use at RIT. An effort to improve the chamber was taken prior to extensive testing. Firstly, there was a thick, 0.5-1mm polymer film along all the sidewalls and showerhead that was cracking and introducing particulates into the chamber. This polymer film was cleaned from the chamber.

Following the polymer removal, it was noticed that there was a Teflon screw cap as opposed to a polycarbonate screw cap in the showerhead as depicted in point A of Figure 4.2. Teflon under RF conditions has a significantly different inductance than polycarbonate, this significantly contributed to etch non-uniformities that were reported prior to this work. The chamber was then seasoned with an Applied Materials proprietary recipe which due to copyright cannot be replicated here. The chamber seasoning is important as it places polymer on the sidewalls, this polymer deposition does multiple things [81, 82]. Firstly, during any standard etch polymer is going to be deposited on the sidewalls of the chamber, however in a unseasoned situation the etch rate for a given etch will drop as some gas flow is depleted to react with the surface of the chamber as

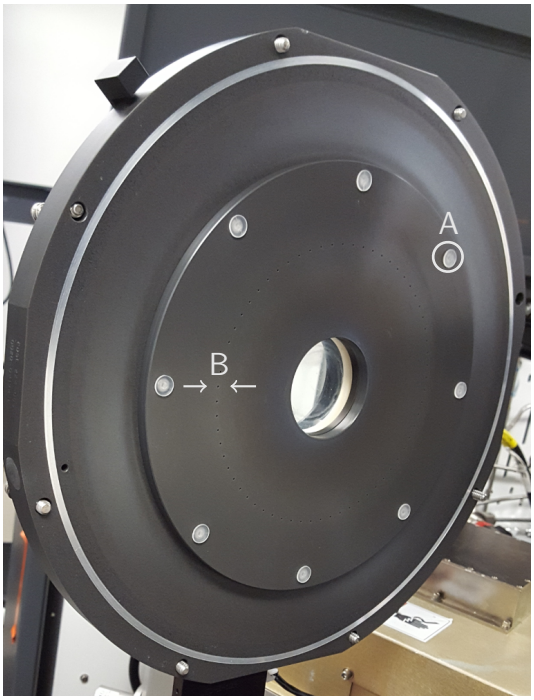

Figure 4.2: MERIE showerhead. Point (A) is where the screwcap was replaced. Point(B) roughly approximates the width of a ring formed around the showerhead pinholes that occurs from proper seasoning.

opposed to the wafer. When the sidewalls of the chamber are passivated with polymer then the gases tend to not interact with the sidewalls of the chamber providing more available etchant for the wafers. Prior to cleaning the sidewall polymer with its cracking and other non-uniformities likely provided a larger surface area for polymer to continue to form as if the chamber had no polymer at all, that is however speculation. A rule of thumb for seasoning RIT's chamber was that the polymer should not be formed within 1cm of the pinholes in the showerhead as depicted by point B in Figure 4.2, this resulted in a over-seasoned chamber and decreased rates. Following this, the clamping pressure was adjusted and leveled. The clamp ring is depicted in Figure 4.3 in both the lifted(Figure 4.3a) and clamped(Figure 4.3b) positions, any irregular clamping pressure would produce a left-right or right-left gradient on the wafer due to uneven helium cooling which was producing non-uniformities in the past.

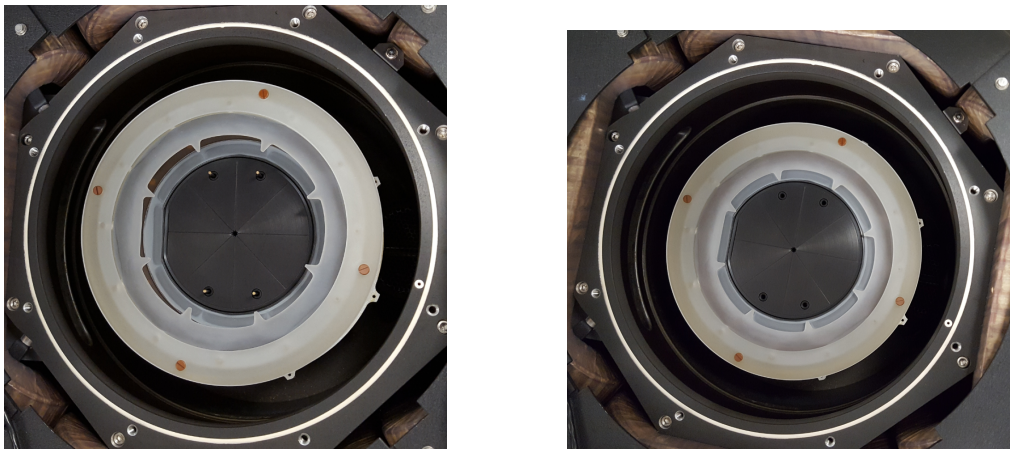

(a) **(b)**

Figure 4.3: MERIE Chamber chuck in both the lifted(a) and clamped(b) positions.

Preliminary etching was then performed based on literature as shown in table 4.3 [34, 42–44, 47, 48, 50, 83–85]. The Literature suggested that the conditions of etch number 3 would be the most anisotropic but with low resist selectivity and etch number 2 would be isotropic but have high resist selectivity. As expected etch number 2 had the a high oxide etch rate with a low resist etch rate. The degree of anisotropy was not directly measured, but as stated previously the literature indicates that the etch should be more isotropic. Also as expected etch number 3 had a lower oxide etch rate and higher resist etch rate. We can conclude that etch number 3 is likely a better candidate for long term use as a new standard recipe in place of RIT's current standard MERIE oxide etch recipe.

With the chamber now having a better and more stable process the proposed screening experiment could proceed forward. This process was to be performed over a number of different films in the proposed process flow namely; Si, Si_3N_4, SiO_2, SiO_xF_y, photoresist, and SOC. The experiment was to follow the industry technique known as couponing whereby a sample of each film was placed on a carrier wafer and all exposed to the plasma at the same time such that they were all under the same conditions for a given run [86]. This however required further process improvements to the etch chamber.

Etch	1	2	3	4	5	RIT STD
Power(W)	500	500	500	500	400	500
Pressure(mTorr)	250	250	250	250	200	250
Mag(G)	50	60	60	60	30	40
CHF_3	36	30	15	25	75	100
CF_4	18	15	30	50	15	50
Ar	120	100	100	100	125	0
O_2	0	0	0	0	0	10
Oxide Rate(Å min^{-1})	1458	2076	2215	2786	1256	1529
Oxide %	0.1	0.35	0.23	0.9	0.6	0.63
Oxide Range(Å min^{-1})	67	157	116	284	165	53
Resist Rate(Å min^{-1})	480	495	896	965	53	–
Resist %	3	0.61	1.49	2.3	1.2	–
Resist Range(Å min^{-1})	412	130	234	535	835	–
Selectivity(Resist:Oxide)	1:3	1:4	9:22	5:14	1:26	–

Table 4.3: Extrapolated data for preliminary screening etch

A process to assure that pieces could be used in the chamber on a carrier wafer was needed. All prior work had been done using full wafers. This posed interesting problems, as patterned pieces were showing thermal instabilities as a result of not being in direct contact with the helium intended to cool the wafer. Figure 4.4 illustrates the thermal problems created in resist features. Both Figures 4.4a and 4.4b are near a patterned resist edge. Figure 4.4a shows early stages of reticulation(burning resist) and Figure 4.4b shows the near final progression of this degradation.

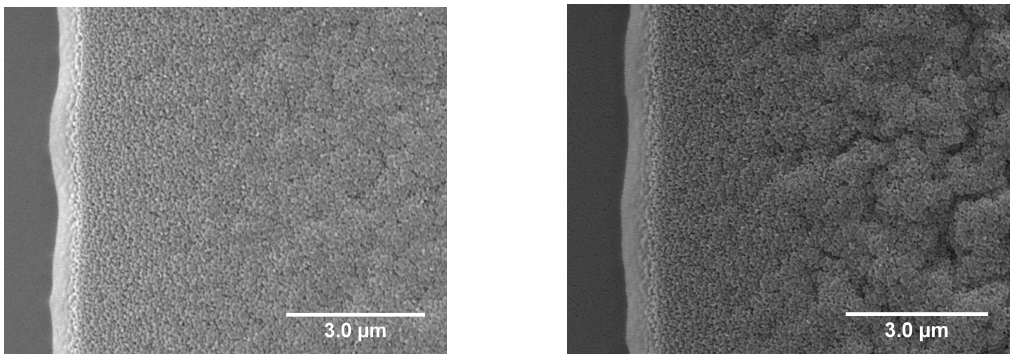

(a) **(b)**

Figure 4.4: SEM images of reticulated resist. Image (a) shows early stages of reticulation whereas image (b) shows later stages of reticulation and/or higher temperature exposure

This reticulation proved to be a significant problem in the striping of the resist once the wafer was removed from the chamber; this is largely also why the helium cooling chuck was adjusted. The clamping pressure/differential cooling caused reports of burning resist prior to this work which is why aluminum hardmasks were recommended and used in prior work [19]. It is believed that the photoresist started to react with the polymer being deposited along with the outgassing of solvent at higher temperatures producing a hard to remove film. As such a polymer removal/descum recipe was developed as shown in table 4.4, this is intended to be run prior to samples leaving the chamber such that the polymer surface does not become hydrogen-terminated. To resolve the heating issue, the carrier wafer should be coated with a layer of photoresist and hardbaked. This photoresist layer allows for better sample adhesion to the surface as opposed to a Si-Si surface with native air-gaps. The clamp and helium also create some bow in the wafer, if the pieces are too large to lay flat on the surface of the bowed carrier wafer the helium pressure can be turned down a little bit which would decrease the bow angle.

Power(W)	300
Pressure(mTorr)	300
Mag(G)	50
Ar	12
O_2	59

Table 4.4: Polymer descum recipe

After the cooling issues were resolved the blanket oxide etch for uniformity as described in section 3.2 and outlined in table 3.1 was performed on 15, 6" wafers, the data is represented in Figures 4.5 and 4.6. The data was normalized for concentration of gas flows within the test. The data was then evaluated for high etch rate and uniformity where points e,i,m and q (circled) were determined to be the best given both factors from both figures. This roughly produces a ideal etching conditions to be a ratio of 2 CF_4 : 2 CHF_3 : 1 C_2F_6 as depicted by a triangle on both graphs. Previous data from etches numbered 2 and 3 (from table 4.3) and literature suggested that a 2:1 ratio of CF_4 to

CHF_3 is good and likely anisotropic. If we rework this into the ratio, we achieve a new ratio of 4 CF_4 : 2 CHF_3 : 1 C_2F_6 . These two ratios are the best candidates going forward for further testing for high anisotropic etching at a reasonable rate with good uniformity.

Similarly, points a,g and j show that an ok etch rate can be achieved without CF_4 with good uniformity. With CF_4 being the primary etchant for Si_3N_4 removing it is a good idea for the mandrel strip etch (section 3.1.9). CF_4 and C_2F_6 are both unsaturate etchants which also preferentially etch SiO_2 over Si_3N_4. Normally in a standard CHF_3 $/CF_4$ mixture designed for etching SiO_2 a polymer film would preferentially grows on Si then Si_3N_4 followed by SiO_2 [34, 42, 75, 87–90]. This usually would mean that there isnt a problem with striping the SiO_2 over Si_3N_4 but there is generally very low selectivity between the two in this chemistry. As such, a etch should be designed with only unsaturate etchants to improve selectivity to nitride. Based on the data, provided in the figures, a 1:4 and 1:2 ratio should be investigated for both CHF_3 and C_2F_6 being the primary/larger etchant concentration for uniformity and selectivity to Si_3N_4 and SOC. Following this there were plans to move to the couponing process however due to time and funding constraints this was not performed.

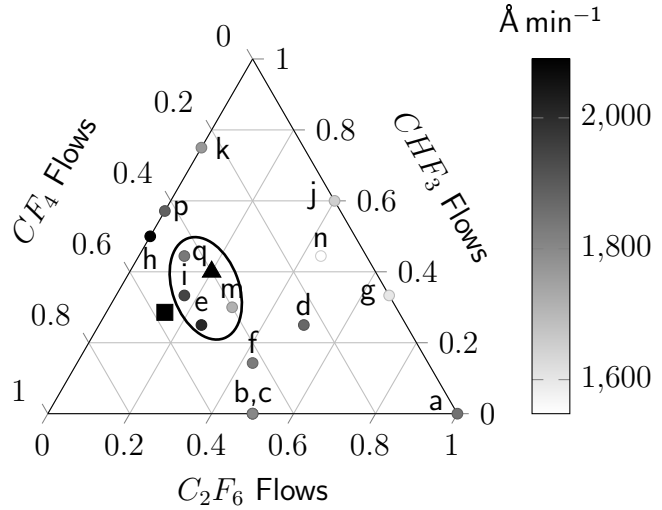

Figure 4.5: Normalized rate data for the etch test, with data shown in Å min^{-1}, higher is preferred.

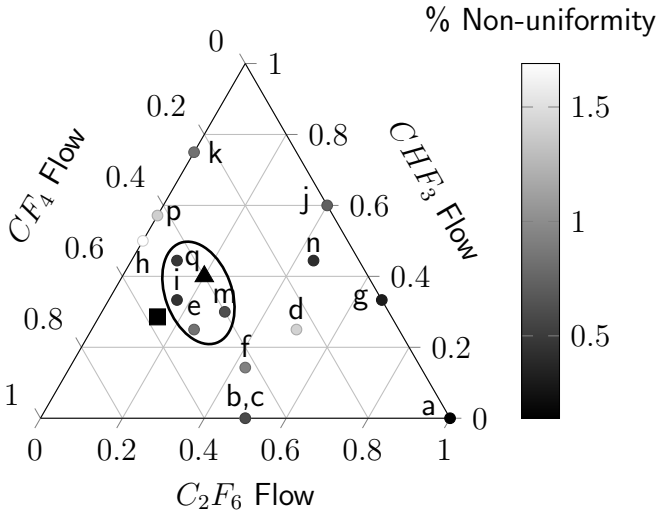

Figure 4.6: Non-uniformity data for the etch test, lower is better or more uniform.

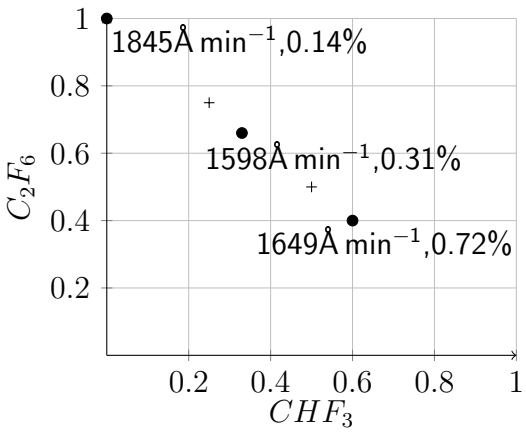

Figure 4.7: C_2F_6 vs CHF_3 data, points(•) shown with Å min^{-1} and non-uniformity percentage. Points(+) are extrapolated ratios.

Conclusions

A path forward for achieving a mandrel etch and strip(Sections 3.1.6 and 3.1.9) with gas flow ratios of 4 CF_4 : 2 CHF_3 : 1 C_2F_6 and 4 C_2F_6 : 1 CHF_3 was derived. In achieving these new gas flow ratios many improvements to RIT's MERIE dry etcher were performed to improve uniformity developing a new standard process for oxide etching. By not including CF_4 in the mandrel strip etch it is highly probable that a mandrel could be stripped without etching the Si_3N_4 spacers present. If this is not the case, further developments need to be made to have a higher etch rate SiO_2 film such as SiO_xF_y as with the process developed through this work does not allow for a BOE strip of the SiO_2 for fear of a liftoff removal of the SOC fin hardmask during either the etch or rinse steps.

With RIT continuing to improve its CMOS process to produce FinFETs it will be able to educate the next generation of process engineers with up-to-date processes for a brighter future. This work provides a good starting point to further that goal. The problems with achieving SADP at RIT have been outlined in a stepwise fashion, with key points highlighted and concerns addressed. A MERIE etcher was brought back into proper specifications such that the process can proceed with highly uniform etches to improve die yield for the process and future unknown steps that require it.

Looking towards the future, RIT's PECVD nitride on the P5000 is getting an upgrade to a number of its systems allowing it to be uniform again. With this, the process outlined in this work can be fully realized. One of the major benefits of this process is that once refined the process can be preformed without breaking vacuum to atmosphere. This process can further be expanded to a SAQP process with a little extra prep-work. If a SOC/nitride layer were deposited first prior to the SOC/oxide then continue the process till the nitride layer is reached, the process can be repeated in a similar fashion as depicted by Figure 5.1. This would produce even smaller features that could be used for introducing the next generation of students to FinFET technology.

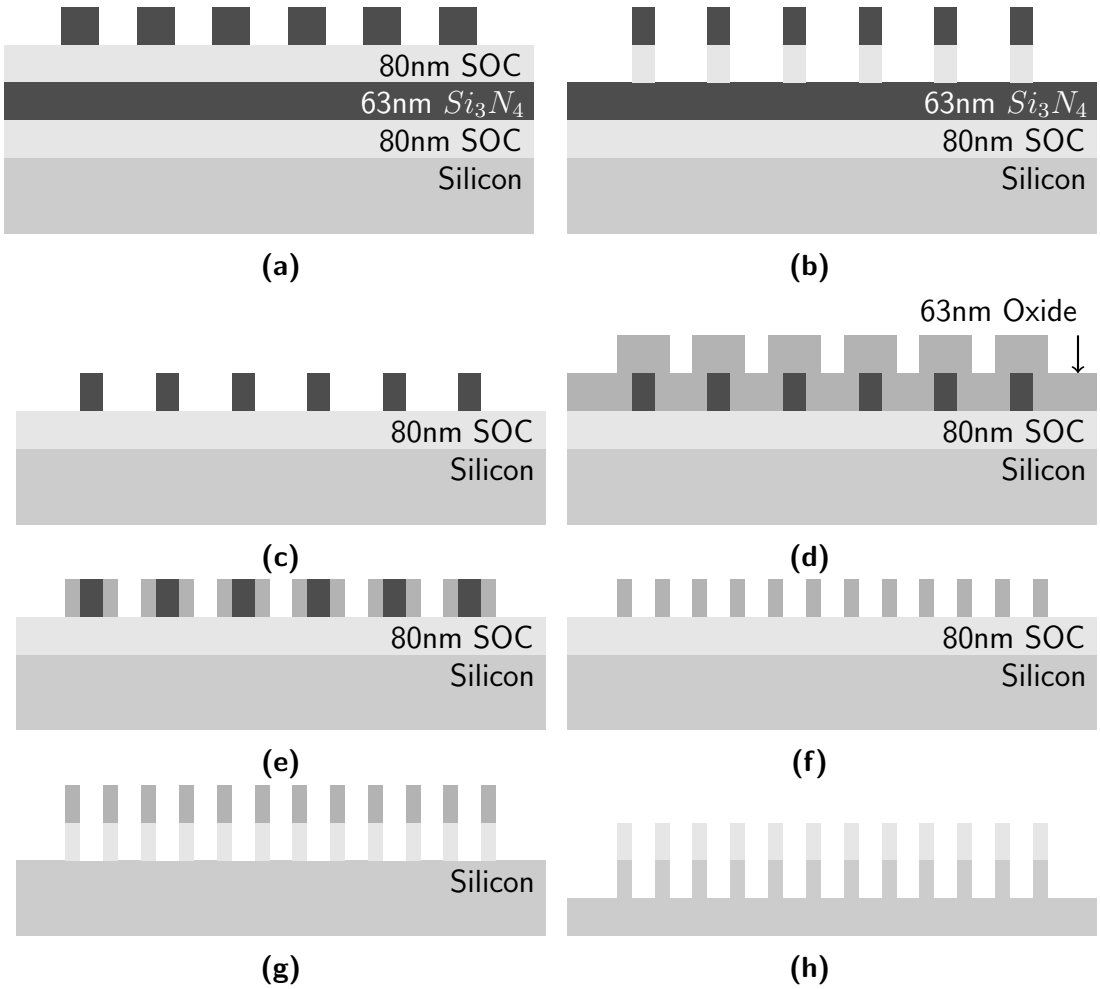

Figure 5.1: Process flow for changing SADP into SAQP after mandrel removal(a). The nitride is trimmed and etched into the SOC(b). The pattern is then used to form a new mandrel in the bottom nitride(c) preformed similarly to the mandrel etch(Section 3.1.6). Oxide is then deposited as a spacer material(d), and spacer etched(e). The nitride mandrel is then stripped(f) preformed similarly to the mandrel strip(Section 3.1.9). The pattern is then imparted into the SOC(g) and then further imparted into the silicon to form fins(h).

References

[1] L. Fuller, "Firsts for microelectronic engineering," Firsts for Microelectronic Engineering. [Online]. Available: https://people.rit.edu/lffeee/May2001.pdf

[2] L. Fuller, K. Hesler, S. Kurinec, R. Lane, R. Pearson, B. Smith, and I. Turkman, "A new program at rit: master of engineering in microelectronics manufacturing engineering," *Proceedings., Eighth University/Government/Industry Microelectronics Symposium*, 1989.

[3] J. Gardner, J. Conners, L. Fuller, W. Gross, and D. Price, "A student-run ic factory at rit," *Proceedings., Eighth University/Government/Industry Microelectronics Symposium*, p. 118–122, 1989.

[4] L. Fuller, "The manufacture of cmos integrated circuits in a university microelectronics laboratory," *Proceedings of the Thirteenth Biennial University/Government/Industry Microelectronics Symposium (Cat. No.99CH36301)*, 1999.

[5] S. Bhaskaran, "Design of rit's sub-micron cmos process," Master's thesis, Rochester Institute of Technology, 2000.

[6] I. Puchades, "Development and characterization of a sub-micron cmos process as an educational tool at rit," Master's thesis, Rochester Institute of Technology, 2001.

[7] M. Aquilino, "Development of deep submicron cmos process for fabrication of high performance 0.25 nm transistors," Master's thesis, Rochester Institute of Technology, 2006.

[8] S. Parikh, "Manufacturing design and fabrication of 100 nm (leff) cmos devices," Master's thesis, Rochester Institute of Technology, 2014.

[9] C. Amareshbabu, "Modeling, simulation and fabrication of 100 nm (leff) high performance cmos transistors," Master's thesis, Rochester Institute of Technology, 2014.

[10] L. Fuller, "Rit's advanced cmos process integration," RIT's Advanced CMOS Process Integration. [Online]. Available: https://people.rit.edu/lffeee/AdvCmosProcessIntegration.pdf

[11] X. Guo, V. Verma, P. Gonzalez-Guerrero, S. Mosanu, and M. R. Stan, "Back to the future: Digital circuit design in the finfet era," *Journal of Low Power Electronics*, vol. 13, no. 3, p. 338–355, Jan 2017.

[12] A. Karel, M. Comte, J.-M. Galliere, F. Azais, and M. Renovell, "Resistive bridging defect detection in bulk, fdsoi and finfet technologies," *Journal of Electronic Testing*, vol. 33, no. 4, p. 515–527, 2017.

[13] C. Branislav, "Development of a fully-depleted thin-body finfet process," Master's thesis, Rochester Institute of Technology, 2004.

[14] S. D. Kirby, "Design and fabrication of finfets on soi substrates," Journal of the Microelectronic Engineering Conference, 2003.

[15] M. Kucer, "Dry etching for high aspect ratio silicon fins," Journal of the Microelectronic Engineering Conference, 2014.

[16] B. Lindenau, "Double patterning technique using an aluminum hardmask," Journal of the Microelectronic Engineering Conference, 2008.

[17] E. J. Bowser, "Double patterning isolated and dense features with an asml pas 5500 i-line stepper," Journal of the Microelectronic Engineering Conference, 2013.

[18] M. Eggleston, "Development of a lfle double pattern process for te mode photonic devices," Journal of the Microelectronic Engineering Conference, 2017.

[19] S. Omar, "Sidewall spacer lithography and silicon etch for sub-300nm finfets," Journal of the Microelectronic Engineering Conference, 2017.

[20] T. D. Horn, "Amorphous carbon hard mask for multiple patterning lithography," Journal of the Microelectronic Engineering Conference, 2015.

[21] M. Krishnappa, "Process design of spin-on-carbon," Master's thesis, Rochester Institute of Technology, 2017.

[22] H. Tang, J. C. Shearer, L. L. Cheong, N. A. Saulnier, S. A. Sieg, K. Petrillo, A. Metz, and J. C. Arnold, "Reduction of critical dimension difference in litho-etch-litho-etch double patterning process," *Journal of Photopolymer Science and Technology*, vol. 28, no. 1, p. 13–16, 2015.

[23] J. Siebert, P. Brooker, T. Schmoeller, and T. Klimpel, "Analysis of topography effects on lithographic performance in double patterning applications," *Optical Microlithography XXII*, 2009.

[24] H. Y. Y. W. J. K. H. J. L. Yuangsheng Ma, Jason Sweis, "Self-aligned double patterning (sadp) compliant design flow," pp. 8327 – 8327 – 13, 2012. [Online]. Available: http://dx.doi.org/10.1117/12.917775

[25] V. B. H. B. M. M. C. S. V. T. Dusa Mircea, Finders Jo, "Double patterning lithography for 32nm: critical dimensions uniformity and overlay control considerations," *Journal of Micro/Nanolithography, MEMS, and MOEMS*, vol. 8, no. 1, p. 011002, Jan 2009.

[26] K. Nakayama, C. Kodama, T. Kotani, S. Nojima, S. Mimotogi, and S. Miyamoto, "Self-aligned double and quadruple patterning layout principle," *Design for Manufacturability through Design-Process Integration VI*, 2012.

[27] H. Tai, Y.-M. Liao, W.-T. Liu, W.-C. Peng, and T.-H. Ying, "Novel clean concept of advanced patterning film (amorphous carbon) for beyond 2xnm generation self-aligned double-patterning (sadp) process," *ECS Transactions*, vol. 61, no. 3, p. 67–71, 2014.

[28] C. Kodama, H. Ichikawa, K. Nakayama, F. Nakajima, S. Nojima, T. Kotani, T. Ihara, and A. Takahashi, "Self-aligned double and quadruple patterning aware grid routing methods," *IEEE Transactions on Computer-Aided Design of Integrated Circuits and Systems*, vol. 34, no. 5, p. 753–765, 2015.

[29] Y. Chen, X. Xu, Y. Chen, L. Miao, H. Chen, P. Blanco, and C. S. Ngai, "Recessive self-aligned double patterning with gap-fill technology," *Optical Microlithography XXIV*, 2011.

[30] R. Pease and S. Chou, "Lithography and other patterning techniques for future electronics," *Proceedings of the IEEE*, vol. 96, no. 2, p. 248–270, 2008.

[31] W.-Y. Jung, S.-M. Kim, C.-D. Kim, G.-H. Sim, S.-M. Jeon, S.-W. Park, B.-S. Lee, S.-K. Park, J.-S. Kim, L.-S. Heon, and et al., "Patterning with amorphous carbon spacer for expanding the resolution limit of current lithography tool," *Optical Microlithography XX*, 2007.

[32] G. Franz, *Low pressure plasmas and microstructuring technology*. Springer, 2009.

[33] J. L. Vossen and W. Kern, *Thin film processes II*. Academic Press, 1991.

[34] M. A. Lieberman and A. J. Lichtenberg, *Principles of plasma discharges and materials processing*. Wiley-Interscience, 2005.

[35] D. W. Hess, "Plasma–material interactions," *Journal of Vacuum Science & Technology A: Vacuum, Surfaces, and Films*, vol. 8, no. 3, p. 1677–1684, 1990.

[36] M. Ohring, *The materials science of thin films*. Academic Press, 1992.

[37] C. R. Kleijn, "Transport phenomena in chemical vapor deposition reactors," Ph.D. dissertation, TU Delft, 1991.

[38] C. Vallèe, A. Goullet, A. Granier, A. van der Lee, J. Durand, and C. Marlière, "Inorganic to organic crossover in thin films deposited from o2/teos plasmas," *Journal of Non-Crystalline Solids*, vol. 272, no. 2, pp. 163 – 173, 2000. [Online]. Available: http://www.sciencedirect.com/science/article/pii/S0022309300002325

[39] D. W. Hess, "Plasma-enhanced cvd: Oxides, nitrides, transition metals, and transition metal silicides," *Journal of Vacuum Science & Technology A: Vacuum, Surfaces, and Films*, vol. 2, no. 2, p. 244–252, 1984.

[40] K. Kondo, M. Kada, and K. Takahashi, *Three Dimensional Integration of Semiconductors: Processing, Materials, and Applications*. Springer, 2015.

[41] K. Nojiri, *Dry etching technology for semiconductors*. Springer, 2015.

[42] F. D. L. Manos, Dennis M., *Plasma etching: an introduction*. Acad. Press, 1989.

[43] D. L. Flamm, "Mechanisms of silicon etching in fluorine- and chlorine-containing plasmas," *Pure and Applied Chemistry*, vol. 62, no. 9, Jan 1990.

[44] D. L. Flamm and V. M. Donnelly, "The design of plasma etchants," *Plasma Chemistry and Plasma Processing*, vol. 1, no. 4, p. 317–363, 1981.

[45] D. L. Flamm, V. M. Donnelly, and J. A. Mucha, "The reaction of fluorine atoms with silicon," *Journal of Applied Physics*, vol. 52, no. 5, p. 3633–3639, 1981.

[46] K. R. Ryan and I. C. Plumb, "A model for the etching of si in cf4 plasmas: Comparison with experimental measurements," *Plasma Chemistry and Plasma Processing*, vol. 6, no. 3, p. 231–246, 1986.

[47] I. C. Plumb and K. R. Ryan, "A model of the chemical processes occurring in cf4/o2 discharges used in plasma etching," *Plasma Chemistry and Plasma Processing*, vol. 6, no. 3, p. 205–230, 1986.

[48] ——, "Gas-phase reactions of cf3 and cf2 with atomic and molecular fluorine: Their significance in plasma etching," *Plasma Chemistry and Plasma Processing*, vol. 6, no. 1, p. 11–25, 1986.

[49] D. Edelson and D. L. Flamm, "Computer simulation of a cf4 plasma etching silicon," *Journal of Applied Physics*, vol. 56, no. 5, pp. 1522–1531, 1984. [Online]. Available: http://dx.doi.org/10.1063/1.334108

[50] R. DAgostino, *Plasma deposition, treatment, and etching of polymers*. Academic Press, 1990.

[51] K. O. Abrokwah, "Characterization and modeling of plasma etch pattern dependencies in integrated circuits," Ph.D. dissertation, 2006.

[52] I. W. Rangelow, "Critical tasks in high aspect ratio silicon dry etching for microelectromechanical systems," *Journal of Vacuum Science & Technology A: Vacuum, Surfaces, and Films*, vol. 21, no. 4, pp. 1550–1562, 2003. [Online]. Available: http://dx.doi.org/10.1116/1.1580488

[53] A. J. v. Roosmalen, J. A. G. Baggerman, and S. J. H. Brader, *Dry etching for VLSI*. Plenum Press, 1991.

[54] Y. Yang, "Modeling discharge and surface processes in capacitively coupled reactors," Ph.D. dissertation, 2010.

[55] D. Cheng, D. Maydan, S. Somekh, K. Stalder, D. Andrews, M. Chang, J. White, J. Wong, V. Zeitlin, and D. Wang, "Magnetic field-enhanced plasma etch reactor," Jun. 27 1989, uS Patent 4,842,683. [Online]. Available: https://www.google.com/patents/US4842683

[56] T. Schneller, *Chemical solution deposition of functional oxide thin films*. Springer Verlag GMBH, 2016.

[57] User:Smokefoot, "File:solgelcartoon.png," 2013. [Online]. Available: https://upload.wikimedia.org/wikipedia/commons/f/f0/SolGelCartoon.png

[58] Toàn, "Spin-on glass materials and applications in advanced ic technologies," Ph.D. dissertation, University of Twente, 1999.

[59] N. Marins, R. Mota, R. Honda, P. Nascente, M. Kayama, K. Kostov, M. Algatti, N. Cruz, and E. Rangel, "Properties of hydrogenated amorphous carbon films deposited by {PECVD} and modified by {SF6} plasma," *Surface and Coatings Technology*, vol. 206, no. 4, pp. 640 – 645, 2011, carbon-Based Nanostructured Coatings and Composite Films. [Online]. Available: //www.sciencedirect.com/science/article/pii/S0257897211006803

[60] P. G. M. B. S. W. I. G. Y. T. J. B. Jean-Damien Chapon, Catherine Chaton, "Comparison between organic spin-on barc and carbon-containing cvd stack for 65-nm gate patterning," pp. 5753 – 5753 – 12, 2005. [Online]. Available: http://dx.doi.org/10.1117/12.601742

[61] S. Pauliac-Vaujour, P. Brianceau, C. Comboroure, and O. Faynot, "Improvement of high resolution lithography by using amorphous carbon hard mask," *Microelectronic Engineering*, vol. 85, no. 5, pp. 800 – 804, 2008, proceedings of the Micro- and Nano-Engineering 2007 Conference. [Online]. Available: http://www.sciencedirect.com/science/article/pii/S0167931708001263

[62] K.-I. L. K.-D. B. C.-K. B. C.-M. L. H.-S. K. S.-C. M. Young-Sun Hwang, Eung-kil Kang, "Improvement of alignment and overlay accuracy on amorphous carbon layers," pp. 6152 – 6152 – 8, 2006. [Online]. Available: http://dx.doi.org/10.1117/12.656416

[63] M.-S. K. S. B. O. J.-Y. S. N. T. J.-S. K. T. C. Hwan-Sung Cheon, Kyong-Ho Yoon, "Development of spin-on carbon hardmasks with comparable etch resistance to amorphous carbon layer (acl)," pp. 7140 – 7140 – 8, 2008. [Online]. Available: http://dx.doi.org/10.1117/12.804635

[64] V. C. C. L. S. W. M. B. C.-C. C. W. W. P. B. M. L. J. M. J. L. P. T. K. O. C. b. X. Shintaro Yamada, Deyan Wang, "Development of spin-on metal hardmask (somhm) for advanced node," pp. 9425 – 9425 – 11, 2015. [Online]. Available: http://dx.doi.org/10.1117/12.2086005

[65] M. Weigand, V. Krishnamurthy, Y. Wang, Q. Lin, D. Guerrero, S. Simmons, and B. Carr, "Evaluating spin-on carbon materials at low temperatures for high wiggling resistance," in *Advanced Etch Technology for Nanopatterning II*, vol. 8685, Mar. 2013, p. 86850R.

[66] R. E. P. T. L. A. P. R. Andreas Frommhold, Alan G. Brown, "Organic hard masks utilizing fullerene derivatives," pp. 9425 – 9425 – 8, 2015. [Online]. Available: http://dx.doi.org/10.1117/12.2085675

[67] J. Robertson, "Diamond-like amorphous carbon," *Materials Science and Engineering: R: Reports*, vol. 37, no. 4, pp. 129 – 281, 2002. [Online]. Available: http://www.sciencedirect.com/science/article/pii/S0927796X02000050

[68] C. Donnet, A. Erdemir, and J. Robertson, *Tribology of diamond-like carbon films fundamentals and applications*. Springer, 2010.

[69] F. P. Gibbons, A. P. G. Robinson, R. E. Palmer, S. Diegoli, M. Manickam, and J. A. Preece, "Fullerene resist materials for the 32nm node and beyond," *Advanced Functional Materials*, vol. 18, no. 13, pp. 1977–1982, 2008. [Online]. Available: http://dx.doi.org/10.1002/adfm.200701155

[70] J. A. P. R. E. P. A. P. G. R. J. Manyam, M. Manickam, "Plasma etching of high-resolution features in a fullerene molecular resist," pp. 7972 – 7972 – 12, 2011. [Online]. Available: http://dx.doi.org/10.1117/12.879469

[71] I. Materials, "Novel spin-on carbon hardmasks," 2017. [Online]. Available: http://www.microchem.com/pdf/IM-HM-140.pdf

[72] R. E. P. A. P. G. R. A. Frommhold, J. Manyam, "High aspect ratio etching using a fullerene derivative spin-on-carbon hardmask," pp. 8328 – 8328 – 11, 2012. [Online]. Available: http://dx.doi.org/10.1117/12.916426

[73] N. S. N.-a. Y. M. T. H. E. K. K. M. S. H. S. J. T. T. S. Isao Nishimura, Hiroyuki Ishii, "Comparison of single-, bi-, and tri-layer resist process," pp. 5753 – 5753 – 8, 2005. [Online]. Available: http://dx.doi.org/10.1117/12.598367

[74] A. Ravve, *Principles of polymer chemistry*, 3rd ed. Springer, 2012.

[75] H. K. Lee, K. S. Chung, and J. S. Yu, "Selective etching of thick si3n4, sio2 and si by using cf4/o2 and c2f6 gases with or without o2 or ar addition," *Journal of the Korean Physical Society*, vol. 54, no. 5(1), p. 1816–1823, 2009.

[76] J. Yeom, Y. Wu, J. C. Selby, and M. A. Shannon, "Maximum achievable aspect ratio in deep reactive ion etching of silicon due to aspect ratio dependent transport and the microloading effect," *Journal of Vacuum Science & Technology B: Microelectronics and Nanometer Structures*, vol. 23, no. 6, p. 2319, 2005.

[77] Y. Tan, R. Zhou, H. Zhang, G. Lu, and Z. Li, "Modeling and simulation of the lag effect in a deep reactive ion etching process," *Journal of Micromechanics and Microengineering*, vol. 16, no. 12, p. 2570–2575, 2006.

[78] A. Hössinger, Z. Djurić, and A. Babayan, "Modeling of deep reactive ion etching in a three-dimensional simulation environment," *Simulation of Semiconductor Processes and Devices 2007*, p. 53–56.

[79] M. T. Weise, S. C. Selbrede, L. J. Arias, and D. Carl, "Characterization of fluorinated tetra ethyl ortho silicate oxide films deposited in a low pressure plasma enhanced chemical vapor deposition reactor," *Journal of Vacuum Science & Technology A: Vacuum, Surfaces, and Films*, vol. 15, no. 3, p. 1399–1402, 1997.

[80] S. Mizuno, A. Verma, P. Lee, and B. Nguyen, "Improved gap-filling capability of fluorine-doped pecvd silicon oxide thin films," *Thin Solid Films*, vol. 279, no. 1-2, p. 82–86, 1996.

[81] A. Agarwal and M. J. Kushner, "Seasoning of plasma etching reactors: Ion energy distributions to walls and real-time and run-to-run control strategies," *Journal of Vacuum Science & Technology A: Vacuum, Surfaces, and Films*, vol. 26, no. 3, p. 498–512, 2008.

[82] S. Lee, Y.-C. Tien, and C.-F. Hsu, "In situ spectroscopic diagnostics of the influence of chamber wall polymer on oxide etch rate," *MRS Proceedings*, vol. 544, 1998.

[83] S. K. K. Kwon, K. H. K. Kwon, B. W. K. Kim, J. M. P. Park, S. W. Y. Yoo, K. S. P. Park, and Y. K. Kyu, "Characterization of via etching in chf3/cf4 magnetically enhanced reactive ion etching using neural networks," *ETRI Journal*, vol. 24, no. 3, p. 211–220, Jan 2002.

[84] K. Miyake, T. Ito, M. Isobe, K. Karahashi, M. Fukasawa, K. Nagahata, T. Tatsumi, and S. Hamaguchi, "Characterization of polymer layer formation during sio2/sin etching by fluoro/hydrofluorocarbon plasmas," *Japanese Journal of Applied Physics*, vol. 53, no. 3S2, Jan 2014.

[85] S. Lee, J. Oh, K. Lee, and H. Sohn, "Ultrahigh selective etching of si3n4 films over sio2 films for silicon nitride gate spacer etching," *Journal of Vacuum Science & Technology B, Nanotechnology and Microelectronics: Materials, Processing, Measurement, and Phenomena*, vol. 28, no. 1, p. 131–137, 2010.

[86] P. Walker and W. H. Tarn, *Handbook of metal etchants*. CRC Press, 1991.

[87] Y. Zhang, G. S. Oehrlein, and F. H. Bell, "Fluorocarbon high density plasmas. vii. investigation of selective sio2-to-si3n4 high density plasma etch processes," *Journal of Vacuum Science & Technology A: Vacuum, Surfaces, and Films*, vol. 14, no. 4, p. 2127–2137, 1996.

[88] L. Chen, L. Xu, D. Li, and B. Lin, "Mechanism of selective si3n4 etching over sio2 in hydrogen-containing fluorocarbon plasma," *Microelectronic Engineering*, vol. 86, no. 11, p. 2354–2357, 2009.

[89] C. Lele, Z. Liang, X. Linda, L. Dongxia, C. Hui, and P. Tod, "Role of cf2in the etching of sio2, si3n4and si in fluorocarbon plasma," *Journal of Semiconductors*, vol. 30, no. 3, p. 033005, 2009.

[90] S. Dhungana, B. J. Nordell, A. N. Caruso, M. M. Paquette, W. A. Lanford, K. Scharfenberger, D. Jacob, and S. W. King, "Combinatorial survey of fluorinated plasma etching in the silicon-oxygen-carbon-nitrogen-hydrogen system," *Journal of Vacuum Science & Technology A: Vacuum, Surfaces, and Films*, vol. 34, no. 6, p. 061302, 2016.

[91] L. Fuller, "Emcr 731 microelectronics manufacturing i," EMCR 731 Microelectronics Manufacturing I. [Online]. Available: https://people.rit.edu/lffeee/labnotes.htm

[92] A. D. B. Iii and R. A. Gottscho, "Aspect ratio independent etching: Fact or fantasy?" *Japanese Journal of Applied Physics*, vol. 34, no. Part 1, No. 4B, p. 2083–2088, 1995.

[93] D. Tezcan, K. Munck, N. Pham, O. Luhn, A. Aarts, P. Moor, K. Baert, and C. Hoof, "Development of vertical and tapered via etch for 3d through wafer interconnect technology," *2006 8th Electronics Packaging Technology Conference*, 2006.

[94] Ohkuni, Kubota, Nakayama, Eriguchi, Tamaki, Harafuji, Nomura, and Sivaram, "Lissajous electron plasma etching for sub-half micron lsi," *Symposium on VLSI Technology*, 1993.

[95] C. Hedlund, H. Blom, and S. Berg, "Microloading effect in reactive ion etching," *Journal of Vacuum Science & Technology A: Vacuum, Surfaces, and Films*, vol. 12, no. 4, p. 1962–1965, 1994.

[96] K. Abrokwah, P. Chidambaram, and D. Boning, "Pattern based prediction for plasma etch," *The 17th Annual SEMI/IEEE ASMC 2006 Conference*.

[97] M. Gosalvez, Y. Zhou, Y. Zhang, G. Zhang, Y. Li, and Y. Xing, "Simulation of microloading and arde in drie," *2015 Transducers - 2015 18th International Conference on Solid-State Sensors, Actuators and Microsystems (TRANSDUCERS)*, 2015.

Appendix A: RIT Standard Deposition Recipes

	Delay	Deposit	Pump out
Time Max(s)	15	40(for 4000Å)	10
Pressure(Torr)	9	9	Full Open
Temp	390	390	390
RF1(W)	0	205	50
Spacing(mils)	220	220	999
TEOS(sccm)	400	400	0
O_2 (sccm)	285	285	285

Table A.1: PECVD TEOS [91]

Appendix B: RIT Etch Recipes

RF(W)	500
Pressure(mTorr)	250
Magnetic Field (Gauss)	40
CHF_3 (sccm)	100
CF_4 (sccm)	50
O_2 (sccm)	10
Ar (sccm)	0

Table B.1: Old RIT Standard/Baseline Anisotropic Oxide Etch [91]

RF(W)	500
Pressure(mTorr)	250
Magnetic Field (Gauss)	60
CHF_3 (sccm)	15
CF_4 (sccm)	30
O_2 (sccm)	0
Ar (sccm)	100

Table B.2: New RIT Standard/Baseline Anisotropic Oxide Etch

RF(W)	500
Pressure(mTorr)	250
Magnetic Field (Gauss)	60
CHF_3 (sccm)	30
CF_4 (sccm)	60
C_2F_6 (sccm)	15
O_2 (sccm)	0
Ar (sccm)	100

Table B.3: Mandrel Etch

RF(W)	500
Pressure(mTorr)	250
Magnetic Field (Gauss)	60
CHF_3 (sccm)	30
CF_4 (sccm)	0
C_2F_6 (sccm)	15
O_2 (sccm)	0
Ar (sccm)	100

Table B.4: Mandrel Strip

Appendix C: Etch Test Photomask details

A single layer photomask was designed for two purposes. The first purpose was for the etch test outlined in Section 3.2, and the second was to test the process in Section 3.1. The die size was set to approximately 4.5 by 2.75mm, with 2.1-2.5mm long features for cross-sectional SEM analysis. The set of patterns for process flow analysis contains patterns that vary pitch keeping line size at 250nm, 300nm, and 500nm. For the 250nm and 300nm lines other patterns are also present such as a contact cut pattern, a inverse contact cut pattern, back-end metal or gate, that all vary with pitch as well. The etch test design/pattern addresses additional issues, predominantly microloading and Aspect Ratio Dependant Etching (ARDE), while also having some patterns included for erosion and shape. The ARDE patterns use the same 250nm, 300nm, and 500nm values as constants for varying line/space sizes. The microloading features are 6 line/space pairs of same-pitch varying from 250nm to 10µm in 50nm increments. It is worth noting that both ARDE and microloading are predominantly effects seen in a Deep Reactive Ion Etch (DRIE) etch process, on a small scale they are what determine how much overetch is required to clear a film without endpoint detection.

C.1 Aspect Ratio Dependant Etching

ARDE occurs whenever there is more than one pitch on a mask. As such it is very important to take into account when designing a mask. ARDE is predominantly the depletion of etchant to clear-field areas by size or opening [51, 76, 92]. This means that any large clear-field area will clear first before the designed features are etched. Because of this property, if the user does not have a proper idea of how features will etch, the range of conditions for producing a over-etch will be to large and likely result in degraded features. The designed mask pattern is shown in Figure C.1, the effect is shown through Figure C.2. While Figure C.2 shows the ARDE effect with a BOSCH etch, the principle is the same with thinner films and film clearing with over etch.

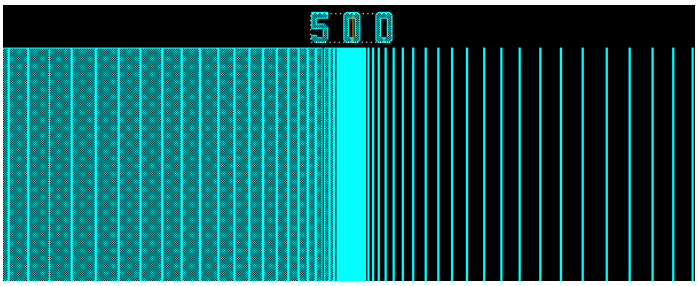

Figure C.1: Positive and Negative ARDE for 500nm features. On the left the space is held constant to 500nm, on the right the line is held constant to 500nm with both varying the other from small to large.

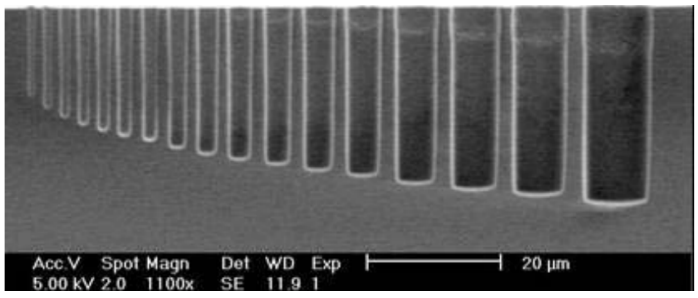

Figure C.2: Positive ARDE from a BOSCH etch [93].

C.2 Microloading

Microloading is another effect that is based on the mask pattern, the mask design for this project is depicted in Figure C.3. The effect is similar to ARDE in that larger clear field(spaces) features deplete etchant more readily than smaller features. In addition features with the same pitch produce a localized concentration gradient as the features that are near the edge of all similar pitch density consume etchant at a higher rate than the center point of the same pitch pattern density. This is best depicted by Figure C.4, the left pattern has a higher density of pattern than the pattern on the right, this produces a large difference in high density patterns as opposed to the low density pattern on the left. [41, 42, 51, 76, 77, 94–97]

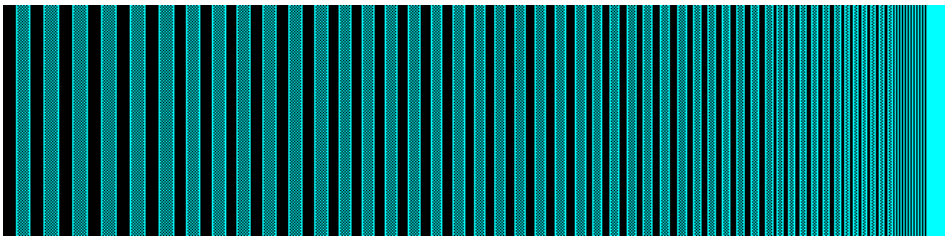

Figure C.3: Sets of 6 bars equal pitch ranging from 250nm through 10µm in steps of 50nm

Figure C.4: Affect of microloading for two same-pitch patterns both with the same space size. [97]